Energy Science & Engineering

ORIGINAL ARTICLE OPEN ACCESS

Synergistic Heat Transfer Enhancement in Triangular Enclosures: Hybrid Nanofluid-Porous Wavy Fin Systems Under Magnetohydrodynamic and Radiation Effects

Adil Abbas Alwan[1] | Mohammed Azeez Alomari[2,3] | Ahmed M. Hassan[2] | Ameer K. Salho[4] | Abdellatif M. Sadeq[5] | Faris Alqurashi[6] | Mujtaba A. Flayyih[7] | Mohammad Ghalambaz[8]

[1]Technical College of Engineering, National University of Science and Technology, Nasiriyah, Dhi Qar, Iraq | [2]Department of Mechanical Engineering, University of Al-Qadisiyah, Al-Qadisiyah, Iraq | [3]College of Engineering, University of Warith Al-Anbiyaa, Karbala, Iraq | [4]Republic of Iraq Ministry of Electricity, Al-Qadisiyah, Iraq | [5]Mechanical and Industrial Engineering Department, College of Engineering, Qatar University, Doha, Qatar | [6]Department of Mechanical Engineering, College of Engineering, University of Bisha, Bisha, Saudi Arabia | [7]Biomedical Engineering Department, College of Engineering and Technologies, Al-Mustaqbal University, Hillah, Iraq | [8]Department of Mathematics, Saveetha School of Engineering, SIMATS, Chennai, India

Correspondence: Abdellatif M. Sadeq (as1004958@qu.edu.qa)

Received: 9 April 2025 | **Revised:** 21 July 2025 | **Accepted:** 25 August 2025

Funding: The authors thank Qatar National Library for providing open access funding. The authors are thankful to the Deanship of Scientific Research at the University of Bisha for supporting this study through the Fast-Track Research Support Program.

Keywords: Darcy–Forchheimer | entropy generation | hybrid nanofluid | porous media | radiation | wavy

ABSTRACT

This study numerically investigates thermal transport and fluid dynamics in a triangular cavity filled with a MgO–Ag–H_2O hybrid nanofluid containing an undulating porous fin under electromagnetic field and thermal radiation influences. The governing equations are solved numerically using the Galerkin finite element methodology with Darcy–Forchheimer formulation for porous media representation. A comprehensive parametric study examines the effects of Rayleigh number (Ra, 10^3–10^6), Darcy number (Da, 10^{-5}–10^{-2}), Hartmann number (Ha, 0–80), magnetic field orientation angle (γ, 0°–90°), nanoparticle concentration (φ, 0.005–0.02), heat generation coefficient (λ, 1–5), fin waviness parameter (n_w, 0–6), and radiation intensity factor (Rd, 1–5). The numerical model is validated against established benchmark solutions, demonstrating excellent agreement. Findings demonstrate that increasing Ra substantially improves thermal transport and flow intensity, with the average Nusselt number rising by up to 65% and maximum velocity magnitudes increasing by over 500 times. Electromagnetic field application inhibits thermal transport, with (Nu_{av}) decreasing by 55.6% as Ha increases from 0 to 80. Magnetic field angle optimization shows that $\gamma = 60°$ provides better heat transfer than $\gamma = 0°$ at high Ha values. Nanoparticle addition provides moderate thermal enhancement, with an 11.1% increase in Nu_{av} as φ increases from 0.005 to 0.02, particularly in low-Ra regimes. Radiation effects become most significant at elevated Ra values, with (Nu_{av}) nearly tripling as Rd increases from 1 to 5 at $Ra = 10^6$. Entropy generation analysis reveals that the Bejan number decreases by 98.7% as Ra increases, indicating fluid friction dominance at higher Ra values. These results offer essential guidance for optimizing thermal management systems involving porous structures, nanofluids, and electromagnetic fields.

1 | Introduction

Thermal transport represents a critical challenge across numerous industrial engineering domains. Heat transfer within enclosed spaces constitutes a fundamental consideration in diverse applications, including solar energy collection systems [1–3], electronic cooling technologies [4–6], thermal energy storage facilities [7–10], and building thermal insulation [11, 12]. Enclosed geometries, which may manifest as rectangular [13, 14], triangular [15], square, or complex configurations [16–20], present distinct computational challenges for predicting fluid dynamics and temperature distributions. Consequently, optimizing thermal transport efficiency in these systems remains a significant research priority, driving the implementation of advanced technologies, such as hybrid nanofluids and porous structures [21–26].

Temperature gradient-induced natural convection represents the predominant heat transfer mechanism within enclosed spaces. Beyond natural convection, various factors influence thermal efficiency within cavities, including integrating nanofluids and hybrid nanofluid formulations. These have demonstrated the capacity to enhance thermal conductivity and convective transport, thereby improving system performance [27–29]. Recent thermal transport research has increasingly focused on various nanoparticle applications to enhance heat transfer effectiveness [30–38]. Mehryan et al. [39] investigated convective heat transfer using Al_2O_3–Cu hybrid nanofluids in porous media-filled cavities, employing the finite volume method with the SIMPLE algorithm. Their key contribution was demonstrating a significant reduction in nanoparticle thermal transport capability within porous substrates, with heat transfer rates decreasing by up to 15% compared with the base fluid. This finding challenged the conventional assumption that nanofluids always enhance heat transfer, revealing that in porous media, increased viscosity can outweigh thermal conductivity benefits. Our work differs by examining MgO–Ag hybrid nanofluids in triangular geometries with additional electromagnetic and radiation effects. Hosseinzadeh et al. [40] evaluated thermal performance using mobile fins with various cross-sectional profiles (trapezoidal, concave, parabolic, and convex) immersed in hybrid nanofluids, determining that concave fin geometries yielded maximum thermal transport efficiency. Ghalambaz et al. [41] conducted a theoretical analysis of Cu–water nanofluid convection in a parallelogram enclosure containing a porous medium using the lattice Boltzmann method. Their investigation revealed thermal transport deterioration across all tested configurations, attributed to elevated dynamic viscosity and nanoparticle interference effects, with Nusselt number reductions of 8%–12%. They concluded that nanofluid implementation alone proves inadequate for thermal applications in porous media environments. Our research addresses this limitation by combining nanofluids with multiple enhancement mechanisms, including electromagnetic fields and radiation.

Grosan et al. [42] performed numerical analysis of steady-state natural convection within square porous cavities with nanofluids and internal heat generation. Their research established that porous media saturated with nanoparticle-enhanced fluids improved thermal transport processes, notably when nanoparticle thermal conductivity exceeded that of the porous substrate. Meanwhile, Sheikholeslami [43] numerically investigated radiative heat transfer and natural convection using Fe_3O_4–ethylene glycol nanofluids in porous media using a control volume finite element method, examining geometry and voltage effects on nanofluid properties. The main contribution was demonstrating that magnetic field orientation significantly affects heat transfer patterns, with optimal angles providing 20%–30% enhancement. Our work builds upon this by examining hybrid nanofluids with combined magnetic and radiation effects in triangular enclosures. Sheremet et al. [44] conducted a numerical evaluation of natural convection-driven heat transfer within square porous cavities filled with nanofluids, employing the Tiwari and Das nanofluid model with enhanced empirical correlations for physical property determination to improve computational accuracy. Their key advancement was developing more realistic property correlations that improved prediction accuracy by 15%. Unlike their focus on square cavities with single nanofluids, our investigation examines triangular geometries with hybrid nanofluids under multiple physical effects.

Numerous studies have examined natural convection heat transfer rates under magnetohydrodynamic influences [45–50]. Ghasemi and Siavashi [51] numerically investigated magnetic field effects on natural convection in square porous containers using a parallel Lattice Boltzmann methodology (LBM) code, discovering that magnetic fields consistently reduced Nusselt number values. However, this effect could be modulated through permeability adjustments. Sheikholeslami [52] applied LBM to analyze hydromagnetic convection of nanofluids in open porous cavities. Chamkha and Aly [53] numerically evaluated combined magnetic field and nanofluid effects on natural convection along vertical permeable surfaces with heat generation, absorption, and injection/suction phenomena. Ghaly [54] conducted a numerical investigation of free-convection heat and mass transfer near isothermal surfaces, examining the integrated effects of buoyancy, radiation, and transverse magnetic fields. This comprehensive parametric analysis assessed radiation and magnetic parameter influences on velocity distributions, temperature profiles, and concentration patterns. Kumar et al. [55] performed a numerical analysis of magnetic field and viscous nanofluid effects on natural convection across infinite vertical plates while considering the thermal radiation impacts. Their findings have significant applications, particularly for processing magnetic nanomaterials in chemical manufacturing and metallurgical industries.

Recent advances in molecular dynamics simulations have provided deeper insights into nanofluid behavior at the molecular level, enhancing our understanding of thermal transport mechanisms. Studies have demonstrated the importance of molecular-scale interactions in determining macroscopic thermal properties of nanofluids, particularly in complex systems involving multiple phases and external fields. These molecular-level investigations complement continuum-based numerical studies and provide valuable validation for macroscopic models.

This study explores the combined effects of hybrid nanofluids, undulating porous fins, electromagnetic fields, and thermal radiation on natural convection in a triangular enclosure, specifically applied to electronic component cooling. While previous research has focused on individual mechanisms, such as nanofluids or electromagnetic fields, few have examined their combined impacts. The investigation analyzes thermal transport and fluid circulation under parameters, including Rayleigh number, Darcy number, Hartmann number, magnetic field orientation, nanoparticle concentration, radiation intensity, heat generation rate, and fin waviness. The goal is to identify the optimal combinations of parameters to maximize thermal efficiency and to understand the physical mechanisms of heat transfer in this complex system. The key innovation of this study lies in the first-time introduction of the corrugated fin shape parameter (n_w) into hybrid nanofluid systems under electromagnetic field influence, providing a novel approach to thermal enhancement. Ultimately, the study aims to link theoretical models with practical applications, providing insights to enhance thermal management technologies in various industries.

On the basis of a comprehensive literature review and identified research gaps, this study addresses the following key research questions:

1. How do the combined effects of hybrid nanofluids, porous wavy fins, and electromagnetic fields influence natural convection heat transfer in triangular enclosures?
2. What is the optimal combination of parameters (Ra, Da, Ha, γ, φ, λ, n_w, Rd) that maximize heat transfer efficiency while minimizing entropy generation?
3. How does the introduction of the fin waviness parameter (n_w) affect the thermal and fluid flow characteristics in the presence of hybrid nanofluids and magnetic fields?
4. What are the dominant heat transfer mechanisms under different parameter combinations, and how do they transition between conduction and convection regimes?
5. How do radiation effects interact with other enhancement mechanisms to influence overall system performance?

2 | Mathematical Modeling

2.1 | Problem Statement

The investigation employs a triangular enclosure configuration containing a MgO–Ag–H_2O hybrid nanofluid. The inclined upper surface, represented by the blue boundary, constitutes the cooled region, while the horizontal lower boundary, indicated by the red line, forms the heated surface (see Figure 1). The characteristic dimension of the triangular domain is denoted as W. The physical model incorporates gravitational effects (g), indicated by a downward-pointing arrow, and an applied magnetic field (B_0) oriented at angle γ. The enclosure features an internal undulating porous fin influencing flow patterns and thermal transport. Natural convection develops due to the temperature differential between the heated and cooled boundaries. The analysis includes thermal radiation contributions and utilizes the Darcy–Forchheimer formulation to characterize flow behavior through the porous structure.

2.2 | Governing Equations

The mathematical framework consists of equations describing nanofluid natural convection surrounding a porous fin within the triangular enclosure. These formulations account for momentum transfer and thermal transport phenomena across the nanofluid region and the porous domain.

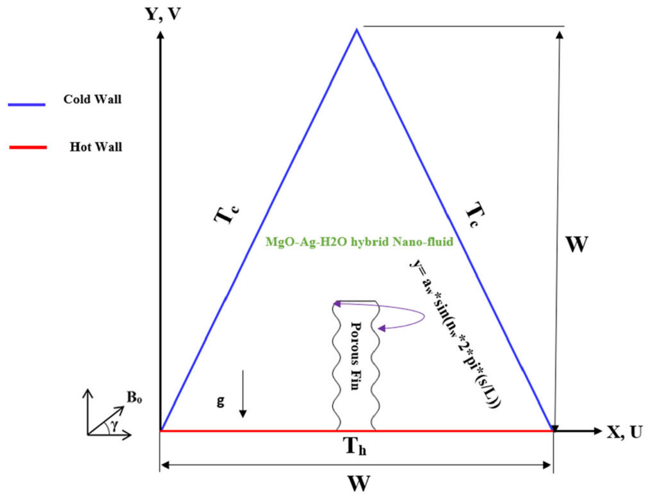

FIGURE 1 | Physical model with boundary conditions.

Nanofluid Region Equations:

The continuity equation ensures mass conservation in the nanofluid [56]:

$$\frac{\partial u_{\mathrm{nf}}}{\partial x} + \frac{\partial v_{\mathrm{nf}}}{\partial y} = 0. \tag{1}$$

Momentum equations, incorporating magnetic field effects [56, 57]:

$$\begin{aligned} u_{\mathrm{nf}} \frac{\partial u_{\mathrm{nf}}}{\partial x} + v_{\mathrm{nf}} \frac{\partial u_{\mathrm{nf}}}{\partial y} &= -\frac{1}{\rho_{\mathrm{nf}}} \frac{\partial p}{\partial x} + \nu_{\mathrm{nf}} \left(\frac{\partial^2 u_{\mathrm{nf}}}{\partial x^2} + \frac{\partial^2 u_{\mathrm{nf}}}{\partial y^2} \right) \\ &+ \frac{\sigma_{\mathrm{nf}} {B_o}^2}{\rho_{\mathrm{nf}}} \sin(\gamma)(v_{\mathrm{nf}} \cos(\gamma) - u_{\mathrm{nf}} \sin(\gamma)), \end{aligned} \tag{2}$$

$$\begin{aligned} u_{\mathrm{nf}} \frac{\partial v_{\mathrm{nf}}}{\partial x} + v_{\mathrm{nf}} \frac{\partial v_{\mathrm{nf}}}{\partial y} &= -\frac{1}{\rho_{\mathrm{nf}}} \frac{\partial p}{\partial y} + \nu_{\mathrm{nf}} \left(\frac{\partial^2 v_{\mathrm{nf}}}{\partial x^2} + \frac{\partial^2 v_{\mathrm{nf}}}{\partial y^2} \right) \\ &+ g \frac{(\rho \beta_{\mathrm{T}})_{\mathrm{nf}}}{\rho_{\mathrm{nf}}} (T - T_{\mathrm{c}}) + \frac{\sigma_{\mathrm{nf}} {B_o}^2}{\rho_{\mathrm{nf}}} \cos(\gamma)(u_{\mathrm{nf}} \sin(\gamma) - v_{\mathrm{nf}} \cos(\gamma)). \end{aligned} \tag{3}$$

The energy equation for the nanofluid includes radiative heat transfer and heat generation [58]:

$$\begin{aligned} u_{\mathrm{nf}} \frac{\partial T_{\mathrm{nf}}}{\partial x} + v_{\mathrm{nf}} \frac{\partial T_{\mathrm{nf}}}{\partial y} &= \alpha_{\mathrm{nf}} \left(\frac{\partial^2 T_{\mathrm{nf}}}{\partial x^2} + \frac{\partial^2 T_{\mathrm{nf}}}{\partial y^2} \right) \\ &- \left(\frac{\partial q_{\mathrm{rx}}}{\partial x} + \frac{\partial q_{\mathrm{ry}}}{\partial y} \right) + \frac{Q}{(\rho C_p)_{\mathrm{nf}}} (T - T_{\mathrm{c}}). \end{aligned} \tag{4}$$

Porous Fin Region Equations:

A similar continuity equation applies to the porous region [59]:

$$\frac{\partial u_{\mathrm{po}}}{\partial x} + \frac{\partial v_{\mathrm{po}}}{\partial y} = 0. \tag{5}$$

The Darcy–Forchheimer model, neglecting inertia terms, describes flow through the porous fin [60]:

$$u_{\mathrm{po}}\frac{\partial u_{\mathrm{po}}}{\partial x}+v_{\mathrm{po}}\frac{\partial u_{\mathrm{po}}}{\partial y}=-\frac{1}{\rho_{\mathrm{nf}}}\frac{\partial p}{\partial x}+\nu_{\mathrm{nf}}\left(\frac{\partial^2 u_{\mathrm{po}}}{\partial x^2}+\frac{\partial^2 u_{\mathrm{po}}}{\partial y^2}\right)-\frac{\mu_{\mathrm{nf}}}{\rho_{\mathrm{nf}}}\frac{u_{\mathrm{po}}}{K}+\frac{\sigma_{\mathrm{po}}{B_{\mathrm{o}}}^2}{\rho_{\mathrm{po}}}\sin(\gamma)(v_{\mathrm{po}}\cos(\gamma)-u_{\mathrm{po}}\sin(\gamma)),\tag{6}$$

$$u_{\mathrm{po}}\frac{\partial v_{\mathrm{po}}}{\partial x}+v_{\mathrm{po}}\frac{\partial v_{\mathrm{po}}}{\partial y}=-\frac{1}{\rho_{\mathrm{nf}}}\frac{\partial p}{\partial y}+\nu_{\mathrm{nf}}\left(\frac{\partial^2 v_{\mathrm{po}}}{\partial x^2}+\frac{\partial^2 v_{\mathrm{po}}}{\partial y^2}\right)+g\frac{(\rho\beta_{\mathrm{T}})_{\mathrm{nf}}}{\rho_{\mathrm{nf}}}(T-T_{\mathrm{c}})-\frac{\mu_{\mathrm{nf}}}{\rho_{\mathrm{nf}}}\frac{v_{\mathrm{po}}}{K}+\frac{\sigma_{\mathrm{po}}{B_{\mathrm{o}}}^2}{\rho_{\mathrm{po}}}\cos(\gamma)(u_{\mathrm{po}}\sin(\gamma)-v_{\mathrm{po}}\cos(\gamma)).\tag{7}$$

The thermal energy conservation equation for the porous domain incorporates effective thermal conductivity:

$$u_{\mathrm{po}}\frac{\partial T_{\mathrm{po}}}{\partial x}+v_{\mathrm{po}}\frac{\partial T_{\mathrm{po}}}{\partial y}=\frac{k_{\mathrm{eff}}}{\rho_{\mathrm{nf}}C_{p_{\mathrm{nf}}}}\left(\frac{\partial^2 T_{\mathrm{po}}}{\partial x^2}+\frac{\partial^2 T_{\mathrm{po}}}{\partial y^2}\right)-\left(\frac{\partial q_{rx}}{\partial x}+\frac{\partial q_{ry}}{\partial y}\right)+\frac{Q}{(\rho C_p)_{\mathrm{nf}}}(T-T_{\mathrm{c}}).\tag{8}$$

Radiative Heat Transfer:

For optically dense boundary layers, the Rosseland [61] formulation is applied to characterize radiative energy flux:

$$q_{rx}=\frac{16T_{\mathrm{c}}^3}{3\beta}\frac{\partial T}{\partial x},\quad q_{ry}=\frac{16T_{\mathrm{c}}^3}{3\beta}\frac{\partial T}{\partial y}.\tag{9}$$

Nondimensionalization:

To enhance analytical generality, the governing equations are converted to dimensionless format using appropriate reference parameters:

$X=\frac{x}{W}$, $Y=\frac{y}{W}$, $U=\frac{uW}{\alpha_{\mathrm{f}}}$, $V=\frac{vW}{\alpha_{\mathrm{f}}}$, $\theta=\frac{T-T_{\mathrm{c}}}{T_{\mathrm{h}}-T_{\mathrm{c}}}$, $P=\frac{pW^2}{\rho_{\mathrm{nf}}\alpha_{\mathrm{f}}^2}$, $Ra=\frac{g\beta_{\mathrm{T}}(T_{\mathrm{h}}-T_{\mathrm{c}})W^3}{\nu_{\mathrm{f}}^2}Pr$, $Pr=\frac{\nu_{\mathrm{f}}}{\alpha_{\mathrm{f}}}$, $Da=\frac{K}{W^2}$, $\lambda=\frac{QW^2}{k}$, $Rd=\frac{4\sigma_{\mathrm{B}}T_{\mathrm{c}}^3}{k\beta}$, $Ha=B_{\mathrm{o}}W\sqrt{\frac{\sigma_{\mathrm{nf}}}{\rho_{\mathrm{nf}}\nu_{\mathrm{nf}}}}$.

The resulting nondimensional equations for both the nanofluid and porous regions are presented, incorporating key dimensionless numbers, such as the Rayleigh number (Ra), Prandtl number (Pr), Darcy number (Da), and Hartmann number (Ha).

- For hybrid nanofluid

$$\frac{\partial U_{\mathrm{nf}}}{\partial X}+\frac{\partial V_{\mathrm{nf}}}{\partial X}=0,\tag{10}$$

$$U_{\mathrm{nf}}\frac{\partial U_{\mathrm{nf}}}{\partial X}+V_{\mathrm{nf}}\frac{\partial U_{\mathrm{nf}}}{\partial Y}=-\frac{\partial P}{\partial X}+\frac{\mu_{\mathrm{nf}}}{\rho_{\mathrm{nf}}\nu_{\mathrm{f}}}Pr\left(\frac{\partial^2 U_{\mathrm{nf}}}{\partial X^2}+\frac{\partial^2 U_{\mathrm{nf}}}{\partial Y^2}\right)+\frac{\mu_{\mathrm{nf}}}{\rho_{\mathrm{nf}}\nu_{\mathrm{f}}}Pr\,Ha^2\sin(\gamma)(V_{\mathrm{nf}}\cos(\gamma)-U_{\mathrm{nf}}\sin(\gamma)),\tag{11}$$

$$U_{\mathrm{nf}}\frac{\partial V_{\mathrm{nf}}}{\partial X}+V_{\mathrm{nf}}\frac{\partial V_{\mathrm{nf}}}{\partial X}=-\frac{\partial P}{\partial Y}+\frac{\mu_{\mathrm{nf}}}{\rho_{\mathrm{nf}}\nu_{\mathrm{f}}}Pr\left(\frac{\partial^2 V_{\mathrm{nf}}}{\partial X^2}+\frac{\partial^2 V_{\mathrm{nf}}}{\partial Y^2}\right)+\frac{(\rho\beta_{\mathrm{T}})_{\mathrm{nf}}}{\rho_{\mathrm{nf}}\beta_{\mathrm{f}}}Ra\,Pr\theta_{\mathrm{nf}}+\frac{\mu_{\mathrm{nf}}}{\rho_{\mathrm{nf}}\nu_{\mathrm{f}}}PrHa^2\cos(\gamma)(U_{\mathrm{nf}}\sin(\gamma)-V_{\mathrm{nf}}\sin(\gamma)),\tag{12}$$

$$U_{\mathrm{nf}}\frac{\partial\theta_{\mathrm{nf}}}{\partial X}+V_{\mathrm{nf}}\frac{\partial\theta_{\mathrm{nf}}}{\partial Y}=\left(\frac{\alpha_{\mathrm{nf}}}{\alpha_{\mathrm{f}}}+\frac{4\alpha_{\mathrm{nf}}Rd}{3\alpha_{\mathrm{f}}}\right)\left(\frac{\partial^2\theta_{\mathrm{nf}}}{\partial X^2}+\frac{\partial^2\theta_{\mathrm{nf}}}{\partial Y^2}\right)+\frac{\alpha_{\mathrm{nf}}}{\alpha_{\mathrm{f}}}\lambda\theta_{\mathrm{nf}}.\tag{13}$$

- For porous layer

$$\frac{\partial U_{\mathrm{po}}}{\partial X}+\frac{\partial V_{\mathrm{po}}}{\partial Y}=0,\tag{14}$$

$$U_{\mathrm{po}}\frac{\partial U_{\mathrm{po}}}{\partial X}+V_{\mathrm{po}}\frac{\partial U_{\mathrm{po}}}{\partial Y}=-\frac{\partial P}{\partial X}+\frac{\mu_{\mathrm{nf}}}{\rho_{\mathrm{nf}}\nu_{\mathrm{f}}}Pr\left(\frac{\partial^2 U_{\mathrm{po}}}{\partial X^2}+\frac{\partial^2 U_{\mathrm{po}}}{\partial Y^2}\right)-\frac{Pr}{Da}U_{\mathrm{po}}+\frac{\mu_{\mathrm{nf}}}{\rho_{\mathrm{nf}}\nu_{\mathrm{f}}}PrHa^2\sin(\gamma)(V_{\mathrm{po}}\cos(\gamma)-U_{\mathrm{po}}\sin(\gamma)),\tag{15}$$

$$U_{\mathrm{po}}\frac{\partial V_{\mathrm{po}}}{\partial X}+V_{\mathrm{po}}\frac{\partial V_{\mathrm{po}}}{\partial Y}=-\frac{\partial P}{\partial Y}+\frac{\mu_{\mathrm{nf}}}{\rho_{\mathrm{nf}}\nu_{\mathrm{f}}}Pr\left(\frac{\partial^2 V_{\mathrm{po}}}{\partial X^2}+\frac{\partial^2 V_{\mathrm{po}}}{\partial Y^2}\right)+\frac{(\rho\beta_{\mathrm{T}})_{\mathrm{nf}}}{\rho_{\mathrm{nf}}\beta_{\mathrm{f}}}Ra\,Pr\theta_{\mathrm{po}}-\frac{Pr}{Da}V_{\mathrm{po}}+\frac{\mu_{\mathrm{nf}}}{\rho_{\mathrm{nf}}\nu_{\mathrm{f}}}PrHa^2\cos(\gamma)(U_{\mathrm{po}}\sin(\gamma)-V_{\mathrm{po}}\sin(\gamma)),\tag{16}$$

$$U_{\mathrm{po}}\frac{\partial\theta_{\mathrm{po}}}{\partial X}+V_{\mathrm{po}}\frac{\partial\theta_{\mathrm{po}}}{\partial Y}=\left(\frac{\alpha_{\mathrm{nf}}}{\alpha_{\mathrm{f}}}+\frac{4\alpha_{\mathrm{nf}}k_{\mathrm{eff}}Rd}{3k_{\mathrm{nf}}\alpha_{\mathrm{f}}}\right)\left(\frac{\partial^2\theta_{\mathrm{po}}}{\partial X^2}+\frac{\partial^2\theta_{\mathrm{po}}}{\partial Y^2}\right)+\frac{\alpha_{\mathrm{nf}}}{\alpha_{\mathrm{f}}}\frac{k_{\mathrm{eff}}}{k_{\mathrm{nf}}}\lambda\theta_{\mathrm{po}}.\tag{17}$$

2.3 | Boundary Conditions and Supplementary Equations

The boundary conditions are carefully selected to represent realistic thermal management scenarios commonly encountered in electronic cooling and industrial heat transfer applications. These conditions simulate practical situations where heat sources require efficient thermal dissipation through natural convection.

The boundary specifications for the dimensionless formulation:

a. Bottom hot wall: $U=V=0,\theta=1$.

   The heated bottom wall with no-slip velocity conditions represents a heat source, such as electronic components or heated surfaces. The constant temperature boundary condition ($\theta=1$) simulates uniform heat flux input, which is typical in practical thermal management systems where consistent heating occurs.

b. Cold walls: $U=V=0,\theta=0$.

The inclined cold walls with no-slip conditions and zero temperature represent heat sinks or ambient cooling surfaces. This boundary condition is physically realistic for applications where the enclosure walls are in contact with cooling systems or ambient environment, providing effective heat removal paths.

These boundary conditions are particularly suitable for this study because they: (1) represent the fundamental configuration for natural convection heat transfer analysis, (2) simulate practical thermal management scenarios where hot sources require cooling through natural convection, (3) provide clear temperature gradients that drive buoyancy-induced flow, (4) are consistent with established natural convection benchmark problems for validation purposes, and (5) allow for meaningful comparison with existing literature on natural convection in enclosures.

The position-dependent Nusselt number is characterized as [15]

$$Nu_L = -\left(\frac{k_{nf}}{k_f} + \frac{4k_{nf}}{3k_f}Rd\right)\frac{\partial\theta}{\partial X}. \tag{18}$$

Average Nusselt number

$$Nu_{av} = \int_0^s Nu_L \, dY. \tag{19}$$

Stream function [62]:

$$U = \frac{\partial\psi}{\partial Y}, \tag{20}$$

$$V = -\frac{\partial\psi}{\partial X}, \tag{21}$$

$$\frac{\partial^2\psi}{\partial X^2} + \frac{\partial^2\psi}{\partial Y^2} = \frac{\partial U}{\partial Y} - \frac{\partial V}{\partial X}. \tag{22}$$

Entropy generation is considered for both fluid friction and heat transfer:

a. Fluid friction entropy generation [63]:

$$s'''_{gen,\mu} = \frac{\mu_{nf}}{T_0}\left[2\left(\frac{\partial U}{\partial X}\right)^2 + 2\left(\frac{\partial V}{\partial Y}\right)^2 + \left(\frac{\partial U}{\partial Y} + \frac{\partial V}{\partial X}\right)^2\right], \tag{23}$$

where $T_0 = \frac{(T_H + T_C)}{2}$.

b. Heat transfer entropy generation [63, 64]:

$$s'''_{gen,h} = \frac{k_{nf}}{T_0^2}\left[\left(\frac{\partial\theta}{\partial X}\right)^2 + \left(\frac{\partial\theta}{\partial Y}\right)^2\right]. \tag{24}$$

c. Nondimensional total entropy generation:

$$\begin{aligned} S'''_{gen} = {} & \frac{k_{nf}}{k_f}\left[\left(\frac{\partial\theta}{\partial X}\right)^2 + \left(\frac{\partial\theta}{\partial Y}\right)^2\right] \\ & + \chi\left[2\left(\frac{\partial U}{\partial X}\right)^2 + 2\left(\frac{\partial V}{\partial Y}\right)^2 + \left(\frac{\partial U}{\partial Y} + \frac{\partial V}{\partial X}\right)^2\right], \end{aligned} \tag{25}$$

where χ (irreversibility factor)

$$\chi = \frac{\mu_{nf} T_0}{k_f}\left(\frac{U_0}{T_H - T_C}\right). \tag{26}$$

The integrated entropy production is determined through

$$\dot{S}_{gen} = \int S'''_{gen} \, dA. \tag{27}$$

The Bejan parameter, which quantifies the proportion of thermal entropy generation relative to total entropy production, is expressed as

$$Be = \frac{S'''_{gen,h}}{S'''_{gen}}. \tag{28}$$

2.4 | Working Fluid Properties

The concentration parameter (φ) of the hybrid nanofluid, comprising Ag and MgO particles dispersed in water, is characterized by

$$\varphi_{nf} = \varphi_{MgO} + \varphi_{Ag}. \tag{29}$$

Table 1 shows the thermophysical properties of water in the normal state and the nanoparticles represented by (MgO and Ag). The following formulas were used to calculate the thermophysical properties of the hybrid nanofluid:

Density (ρ)

$$\rho_{nf} = (1 - \varphi_{nf})\rho_f + \varphi_{MgO}\rho_{MgO} + \varphi_{Ag}\rho_{Ag}. \tag{30}$$

Thermal expansion coefficient ($\rho\beta$)

$$(\rho\beta)_{nf} = (1 - \varphi_{nf})(\rho\beta)_f + \varphi_{MgO}(\rho\beta)_{MgO} + \varphi_{Ag}(\rho\beta)_{Ag}. \tag{31}$$

Specific heat capacity (ρC_p)

$$\begin{aligned} (\rho C_p)_{nf} = {} & (1 - \varphi_{nf})(\rho C_p)_f + \varphi_{MgO}(\rho C_p)_{MgO} \\ & + \varphi_{Ag}(\rho C_p)_{Ag}. \end{aligned} \tag{32}$$

Thermal conductivity ($0 \le \varphi_{nf} \le 0.03$)

$$\frac{k_{nf}}{k_f} = \frac{0.1747 \times 10^5 + \varphi_{nf}}{\begin{array}{c} 0.1747 \times 10^5 - 0.1498 \times 10^6\varphi_{nf} \\ + 0.1117 \times 10^7\varphi_{nf}^2 + 0.1997 \times 10^8\varphi_{nf}^3 \end{array}}. \tag{33}$$

Thermal diffusivity (α)

$$\alpha_{nf} = \frac{k_{nf}}{(\rho C_p)_{nf}}. \tag{34}$$

TABLE 1 | Thermophysical properties of the fluid and two MgO and Ag types of nanoparticles [56, 65, 66].

Properties	Water	MgO	Ag
C_p $(\mathrm{J \cdot kg^{-1} \cdot K^{-1}})$	4179	879	235
k $(\mathrm{W \cdot m^{-1} \cdot K^{-1}})$	0.613	30	429
α $(\mathrm{m^2 \cdot s^{-1}})$	1.47×10^{-7}	95.3×10^{-7}	174×10^{-3}
β $(\mathrm{K^{-1}})$	21×10^{-5}	33.6×10^{-6}	$5.4^{*} \times 10^{-5}$
ρ $(\mathrm{kg \cdot m^{-3}})$	997.1	3580	10,500
μ $(\mathrm{kg \cdot m^{-1} \cdot s^{-1}})$	8.9×10^{-4}	--	--

Viscosity (μ) $0 \le \varphi_{\mathrm{nf}} \le 0.02$

$$\frac{\mu_{\mathrm{nf}}}{\mu_{\mathrm{f}}} = \Big(1 + 32.795\varphi_{\mathrm{nf}} - 7214\varphi_{\mathrm{nf}}^2 + 714600\varphi_{\mathrm{nf}}^3 \\ \Big(-0.1941 \times 10^8 \varphi_{\mathrm{nf}}^4\Big). \tag{35}$$

The composite thermal conductivity of the copper porous fin is determined using the following formula:

$$k_{\mathrm{eff}} = (1 - \varepsilon)k_{\mathrm{p}} + \varepsilon k_{\mathrm{nf}}, \tag{36}$$

where ε is the void fraction of the porous structure, k_{p} is the thermal conductivity of the solid matrix material, and k_{hnf} is the thermal conductivity of the hybrid nanofluid suspension.

Several limitations should be acknowledged in the current study. First, the two-dimensional analysis, while computationally efficient, may not fully capture three-dimensional effects that could be significant in real-world applications. Second, the steady-state assumption neglects transient behaviors that might be important during system startup or under varying operating conditions. Third, the Darcy–Forchheimer model assumes local thermal equilibrium between the fluid and solid phases, which may not hold at very high velocities or with significant temperature differences. Fourth, the nanofluid properties are assumed to remain constant and homogeneous, not accounting for potential nanoparticle agglomeration, sedimentation, or temperature-dependent property variations. Fifth, the magnetic field is assumed to be uniform, while practical implementations may involve nonuniform field distributions. Sixth, viscous heating effects are neglected, which could become significant at very high Hartmann numbers. Finally, the study focuses on specific nanoparticle combinations (MgO–Ag) and a particular base fluid (water), limiting the generalizability to other nanofluid systems. Despite these limitations, the current model provides valuable insights into the fundamental physics and serves as a foundation for more comprehensive future studies.

2.5 | Solution Procedure

The thermal transport characteristics of a hybrid nanofluid experiencing natural convection within a triangular domain incorporating a porous projection are computationally analyzed using Galerkin finite element methodology. This approach necessitates domain discretization, with numerical solution accuracy directly influenced by element density as illustrated in Figure 2. The computational procedure employs an iterative algorithm to determine the nondimensional variables: pressure field (P), velocity vectors (U, V), and temperature distribution (θ). These parameters undergo systematic refinement during each computational cycle until satisfying specific convergence requirements. The convergence assessment utilizes the relative variation of solution variables between sequential iterations, employing the following threshold:

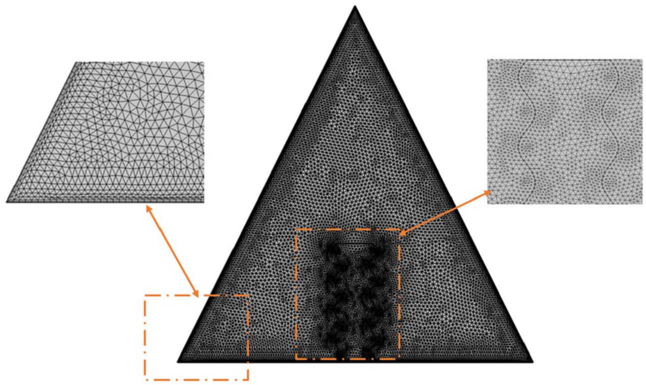

FIGURE 2 | Mesh of the tangle model.

$$\left| \frac{\xi^{i+1} - \xi^{i}}{\xi^{i+1}} \right| \le 10^{-5}. \tag{37}$$

The computational implementation employs adaptive time stepping with an initial step size of $\Delta t = 10^{-4}$, which is dynamically adjusted based on solution stability and convergence rate. The minimum allowable step size is set to 10^{-7} to maintain solution accuracy, while the maximum step size is limited to 10^{-2} to ensure stability. Error tolerance for the iterative solver is maintained at 10^{-8} for pressure calculations and 10^{-6} for velocity and temperature fields to guarantee high precision results.

Multiple validation strategies were implemented to ensure computational accuracy and solution robustness; systematic mesh sensitivity analysis was performed to confirm solution independence from discretization parameters. When equation residuals for continuity, momentum, and energy formulations decrease below 10^{-6}, strict convergence criteria are considered satisfied, with simulations deemed converged. Computational

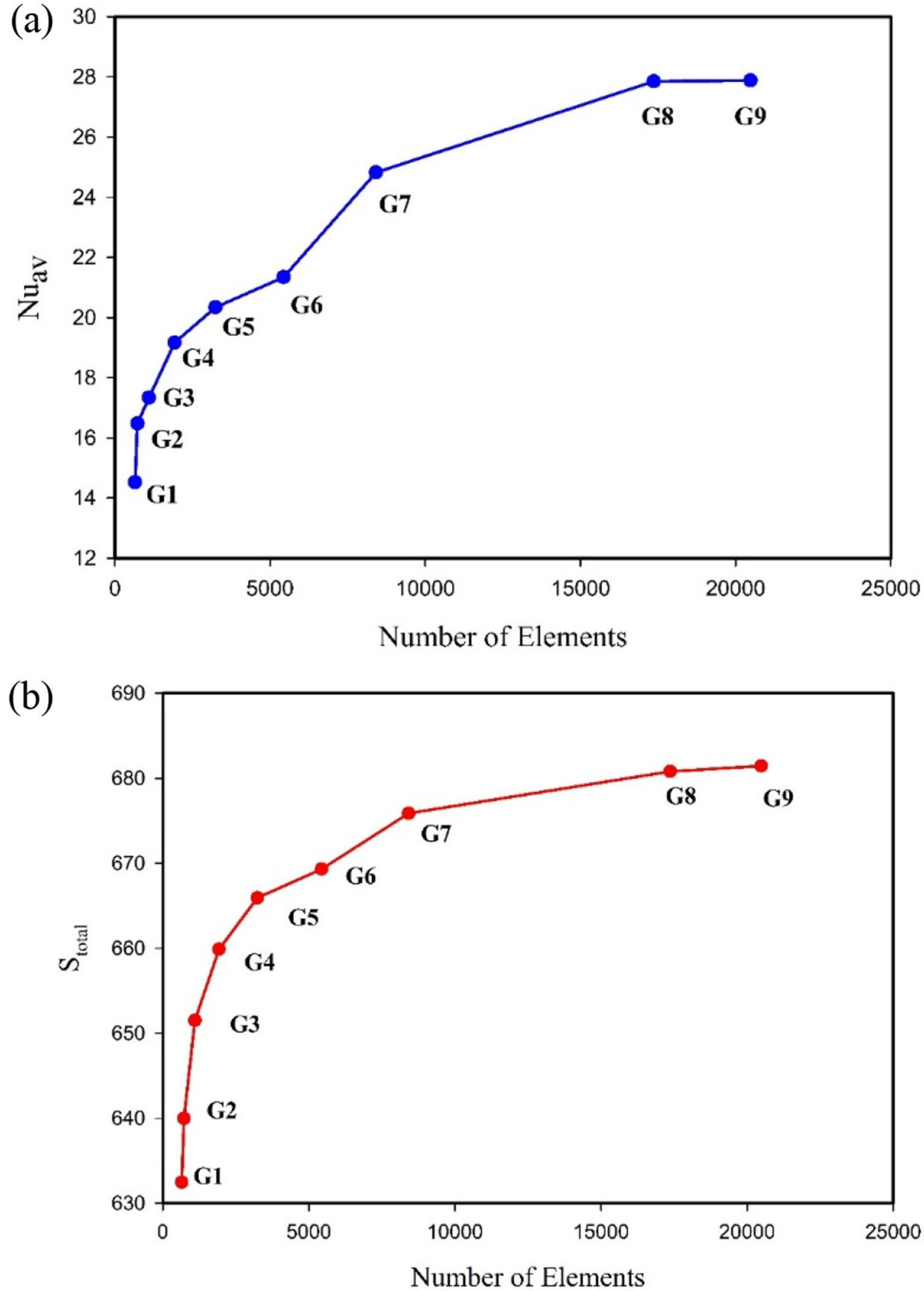

FIGURE 3 | Grid independency (a) for the avarage Nusulet number and (b) for entropy generation.

iterations extend beyond initial convergence to verify solution stability, with critical parameters demonstrating less than 0.01% variation with additional computational cycles.

The simulations were executed on a high-performance workstation equipped with Intel Core i7-10700K processor (3.8 GHz, 8 cores) and 32 GB DDR4 RAM. Average computational time per simulation ranged from 8 to 15 min depending on the complexity of parameter combinations, with higher Rayleigh numbers requiring extended computation due to increased flow complexity. Total CPU time for the complete parametric study was approximately 8 h, with individual cases involving higher Ha values converging faster due to flow suppression effects.

2.6 | Grid Independence Test

A mesh sensitivity analysis was implemented to verify computational accuracy and solution reliability. This evaluation is essential for identifying the optimal discretization density that balances computational resource utilization and solution precision. The assessment was conducted using standardized parameters: $Ra = 10^4$, $Da = 0.001$, $Ha = 5$, $\gamma = 0$, $\varphi = 0.01$, $Rd = 1$, $\lambda = 1$, and $n_w = 4$. Nine discretization configurations were examined, with element counts ranging from 648 to 20,484. The average Nusselt number (Nu_{av}) and total entropy generation (S_{total}) were quantitative indicators for evaluating mesh refinement effects. Progressive mesh enhancement revealed consistent increases in calculated Nu_{av} and S_{total} values, as shown in Figure 3. Relative differences between

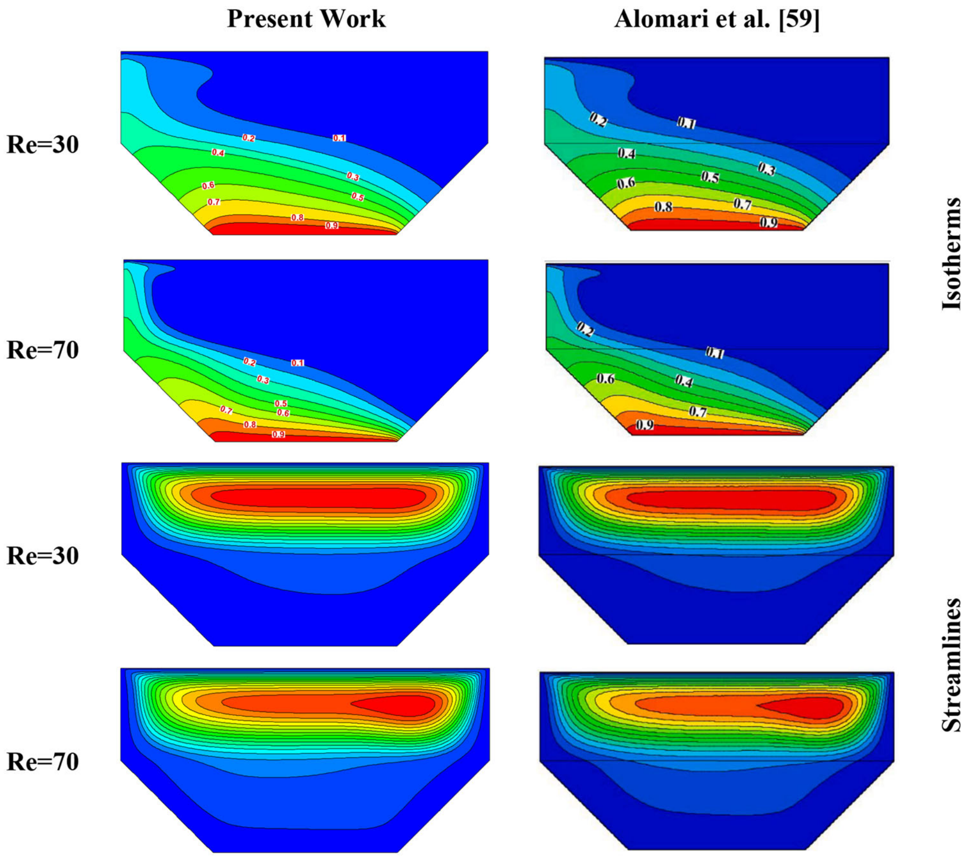

FIGURE 4 | Comparison of present work with Alomari et al. [59].

consecutive mesh refinements were calculated to quantify solution evolution. Analysis demonstrates solution convergence at higher element densities, with the transition from configuration G8 to G9 producing negligible variations in both Nu_{av} (0.1004% difference) and S_{total} (0.096% difference).

2.7 | Model Validation

The computational framework was verified through comparative analysis with multiple published investigations, addressing distinct aspects of the physical system. Initial validation examined electromagnetic field effects by benchmarking against Alomari et al. [59], who investigated inclined magnetic field influences on mixed convection within a lid-driven curvilinear enclosure containing Cu–H_2O nanofluid with a partial porous layer. Figure 4 presents a comparative analysis of flow patterns and temperature contours between our computational implementation and their study. The comparison exhibits strong correlation and appropriate convergence, confirming our model's capability to represent electromagnetic field phenomena accurately.

A second verification was conducted against Basak et al. [60], as illustrated in Figure 5. It compares flow structures and thermal patterns from our simulations with those reported in their investigation of a square cavity containing a porous medium under specific conditions: $Da = 10^{-5}$, $Ra = 10^6$, and $Pr = 0.71$. This assessment further substantiates our model's reliability, demonstrating excellent alignment between our predictions and those of the reference study.

Additionally, we evaluated local Nusselt number distributions between our current investigation and Basak et al.'s [60] work across various Darcy number values, as presented in Figure 6. This comparison validates our model's thermal transport predictions across different porous media permeability conditions. Finally, we compared our calculated flow patterns with the experimental and numerical study by Chen and Cheng [67]. Figure 7 illustrates streamline configurations within a semicircular enclosure, demonstrating good correspondence with our simulations. This comparison is particularly significant as it validates our model against computational and experimental measurements.

3 | Results and Discussions

This section presents the computational findings from our investigation, focusing on parametric effects within the hybrid nanofluid system contained in a triangular enclosure with porous undulating projections. Table 2 summarizes the main physical parameters investigated in this study, along with their ranges and selection criteria.

A fundamental control parameter in this analysis is the Rayleigh number (Ra), varying across (10^3–10^6), which characterizes the intensity of buoyancy-driven convection relative to diffusive transport. (This range was selected to cover the transition from conduction-dominated [$Ra < 10^4$] to convection-dominated [$Ra > 10^5$] heat transfer regimes, representing practical operating conditions in thermal

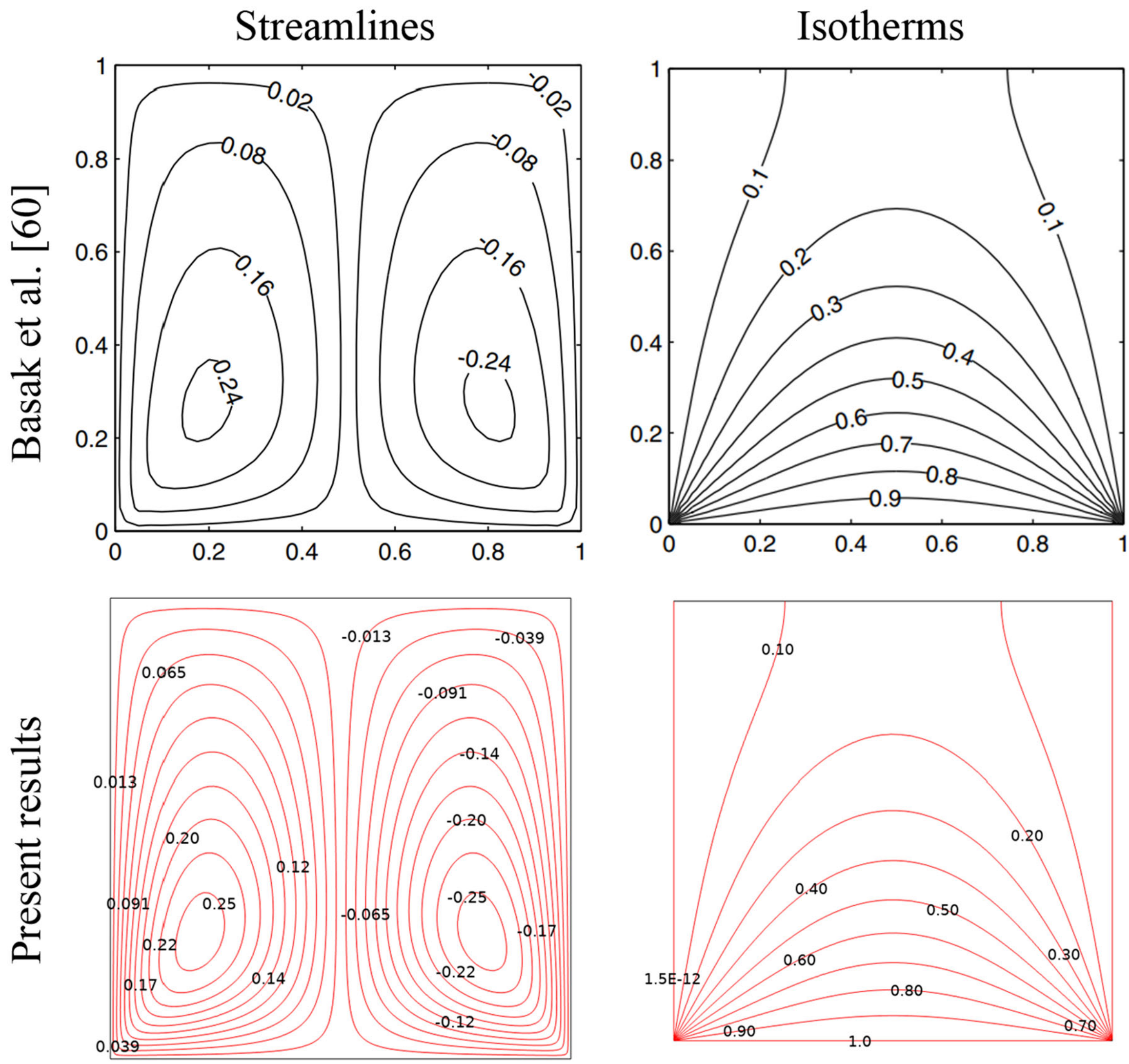

FIGURE 5 | Comparison of isotherms and streamlines between the present study and Basak et al. [60] results.

management systems.) Additionally, Darcy number (Da) values (10^{-5}–10^{-2}) are examined to assess porous medium permeability effects on flow dynamics and thermal transport efficiency. The Da range encompasses materials from tight porous media (low Da) to highly permeable structures (high Da), covering typical industrial porous materials, such as metal foams and packed beds.

To evaluate electromagnetic field influences on system behavior, we investigated Hartmann number (Ha) variations from 0 to 80 and magnetic field orientation angles (γ) ranging from 0° to 90°. (The Ha range was chosen based on achievable magnetic field strengths in practical magnetohydrodynamic applications, while the angular range provides complete directional analysis.) Since the system incorporates radiative effects, thermal radiation parameter (Rd) values between 1 and 5 were analyzed, while internal energy generation/absorption coefficient (λ) was similarly varied from 1 to 5. These ranges represent conditions where radiation becomes significant compared with convection, typical in high-temperature industrial processes.

Regarding nanoparticle loading, individual component concentrations (MgO and Ag) were examined between 0.0025 and 0.01, with cumulative concentrations ranging from 0.005 to 0.02. This concentration range ensures nanofluid stability while avoiding particle agglomeration, based on experimental studies demonstrating optimal enhancement within these limits. This allowed systematic evaluation of particle concentration effects on flow characteristics and temperature distributions. Additionally, we investigated how fin surface waviness (values from 0 to 6) influences thermal transport performance. The waviness parameter $n_w = 0$ represents a straight fin, while $n_w = 6$ indicates maximum practical waviness before manufacturing constraints become prohibitive.

The following analysis examines how these parameters affect key performance metrics Nusselt number, entropy generation, and flow structures. Results are presented through combined visualization of flow patterns, temperature contours, and quantitative performance graphs to provide a comprehensive understanding of the physical phenomena.

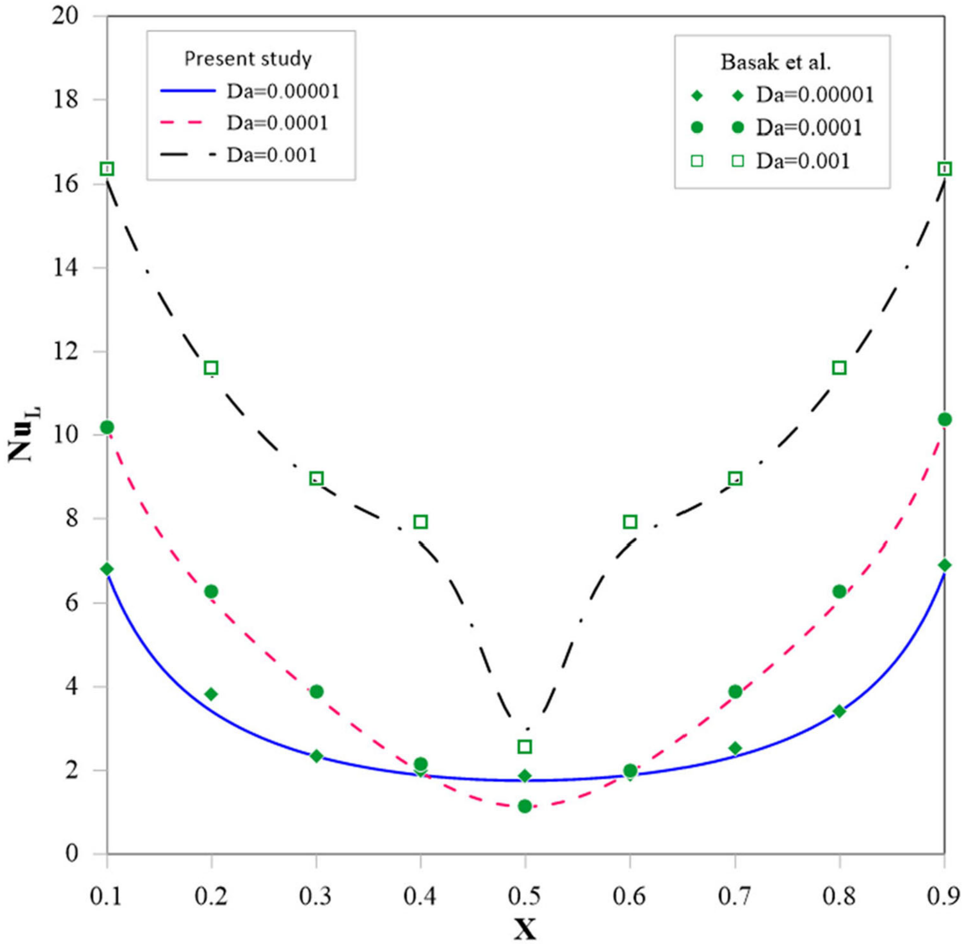

FIGURE 6 | Local Nusselt number distribution comparison between the present study and Basak et al. [60] results.

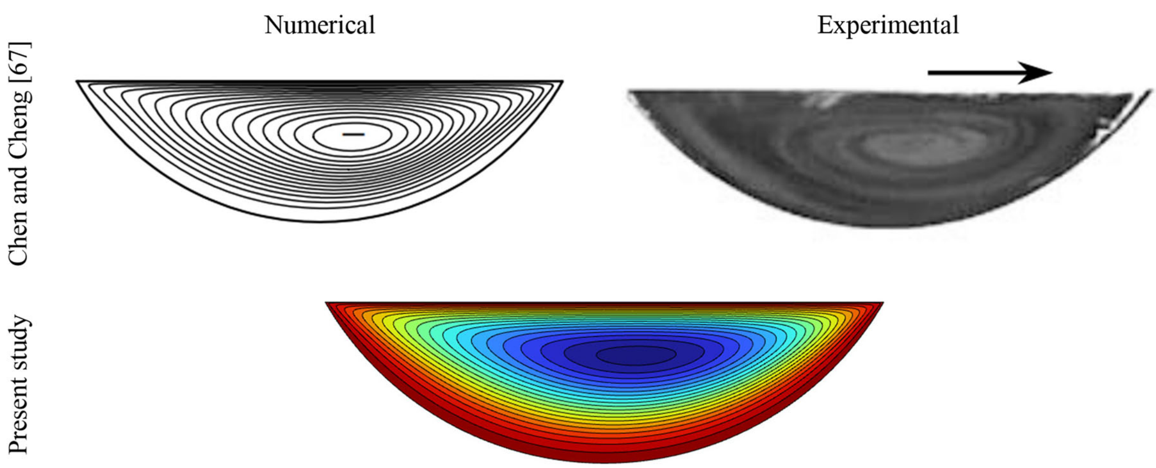

FIGURE 7 | Validation of streamlines results with experimental and numerical rustles of Chen and Cheng [67] results.

3.1 | Effect of Darcy Number

Figure 8 illustrates the combined influence of Rayleigh (Ra) and Darcy (Da) numbers on temperature distribution within the triangular enclosure. As the Rayleigh number increases from 10^3 to 10^6, notable changes in isothermal patterns emerge, demonstrating the progression from conduction-dominated to convection-dominated thermal transport regimes. At lower Rayleigh values, isotherms appear predominantly parallel to the heated lower boundary, indicating thermal conduction as the primary transfer mechanism. With increasing Rayleigh number, significant isothermal distortion becomes apparent near boundary regions, reflecting intensified convective circulation.

The Darcy number, characterizing porous media permeability, substantially influences flow and thermal patterns. At higher Darcy values (10^{-2} and 10^{-3}), reduced flow resistance through the porous structure allows stronger convective currents to

TABLE 2 | Physical parameters and their selection criteria.

Parameter	Range	Selection basis	Physical significance
Rayleigh number (Ra)	10^3–10^6	Literature standards for natural convection studies [15]; covers laminar to transitional regimes	Covers laminar to transitional regimes
Darcy number (Da)	10^{-5}–10^{-2}	Typical porous media permeability range [62]; represents low to high permeability materials	Controls flow resistance in porous medium
Hartmann number (Ha)	0–80	Practical electromagnetic field strengths in industrial applications [20]	Quantifies magnetic field influence on fluid flow
Magnetic field angle (γ)	0°–90°	Complete angular range for comprehensive analysis	Determines magnetic field orientation effects
Nanoparticle volume fraction (φ)	0.005–0.02	Optimal range for nanofluid stability and enhancement [68]; avoids agglomeration	Controls thermal property enhancement
Heat generation parameter (λ)	1–5	Typical internal heat generation in electronic cooling applications [18]	Represents internal energy sources
Fin wavy number (n_w)	0–6	Practical fin design constraints; 0 = straight, 6 = highly wavy	Controls surface area enhancement
Radiation parameter (Rd)	1–5	High-temperature applications where radiation becomes significant [18]	Quantifies the radiative heat transfer contribution

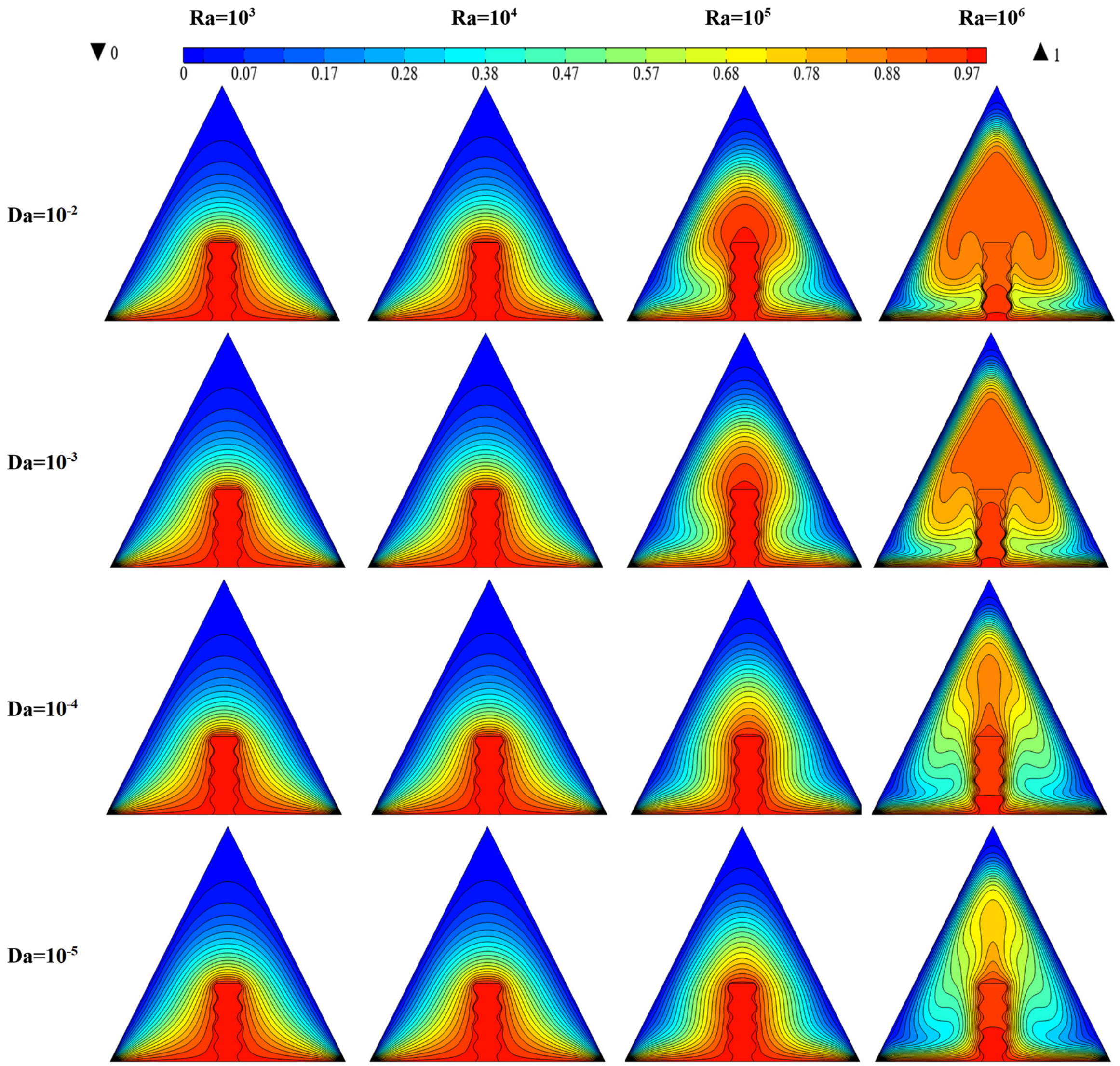

FIGURE 8 | Darcy number effect on isotherms with different values of Rayleigh number at $Ha = 5$, $\gamma = 0$, $\varphi = 0.01$, $\lambda = 1$, and $n_w = 4$.

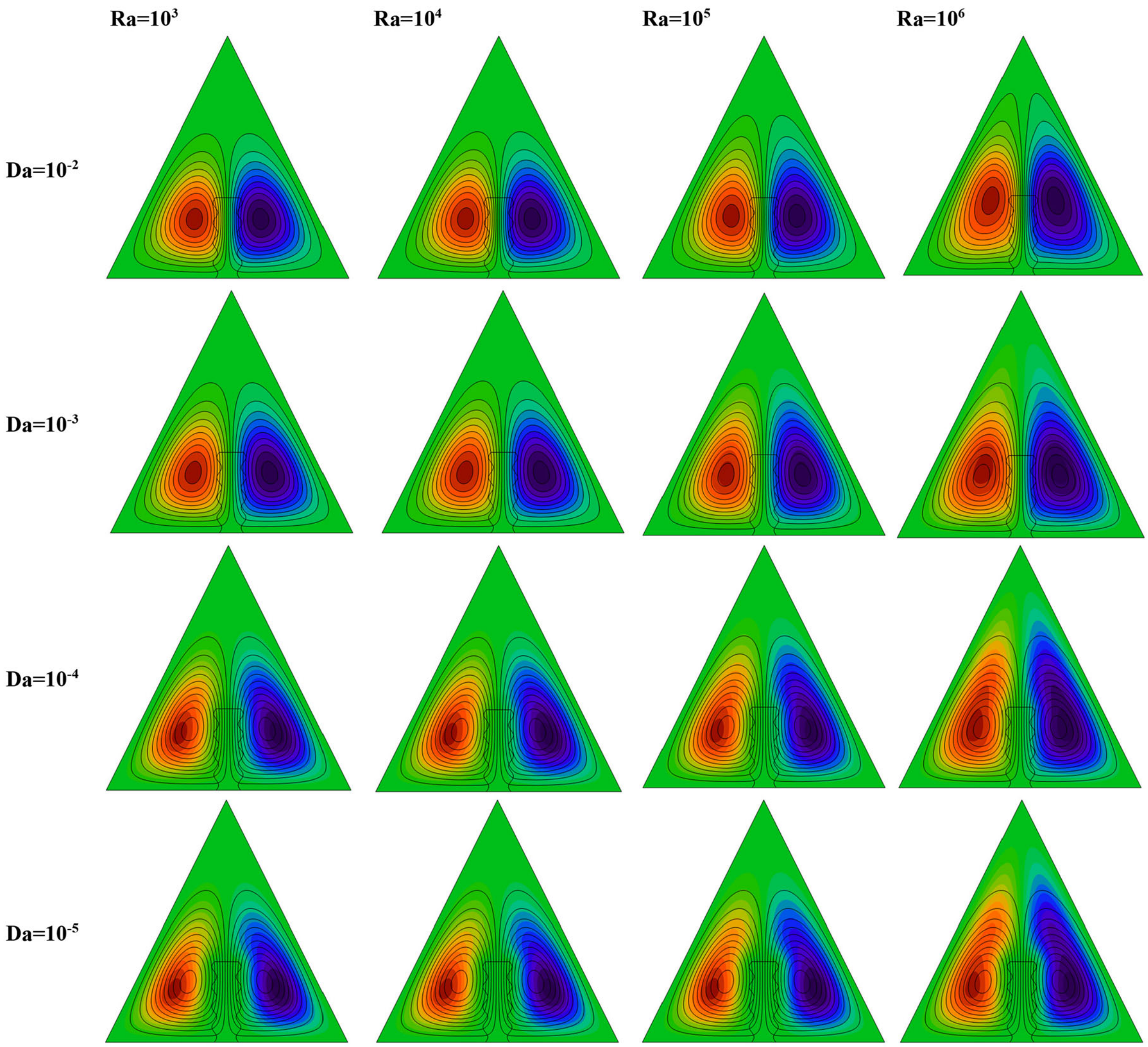

FIGURE 9 | Darcy number effect on streamlines with different values of Rayleigh number at $Ha = 5$, $\gamma = 0$, $\varphi = 0.01$, $\lambda = 1$, and $n_w = 4$.

develop. This phenomenon is particularly evident through pronounced isothermal distortion observed at elevated Rayleigh numbers. Conversely, as the Darcy number decreases to lower values (10^{-4} and 10^{-5}), increased flow resistance through the porous medium suppresses convective transport, resulting in more uniform isothermal distributions even at high-Rayleigh numbers, where convection would typically dominate.

Figure 9 depicts circulation patterns and the combined influence of Rayleigh (*Ra*) and Darcy (*Da*) numbers on flow characteristics within the triangular domain as visualized through streamline distributions. The flow structure exhibits dual circulation zones: a clockwise rotating cell on the left side and a counterclockwise rotating cell on the right. This symmetrical configuration develops from buoyancy-induced upward motion along the heated lower surface and corresponding downward flow along the cooled inclined boundaries. As the Rayleigh number increases from 10^3 to 10^6, these circulation cells intensify, resulting in more concentrated streamline patterns. This concentration directly reflects enhanced buoyancy forces at elevated *Ra* values, strengthening natural convection mechanisms. With increasing Rayleigh number, each circulation zone's core becomes more compact and migrates toward the enclosure corners. The Darcy number significantly influences circulation intensity. At higher *Da* values (10^{-2} and 10^{-3}), reduced flow resistance through the porous structure facilitates stronger and more defined convective patterns. As the Darcy number decreases 10^{-4} and 10^{-5}, convection becomes weaker and more widespread due to the high flow resistance even at high-Rayleigh number values.

Figure 10 illustrates the quantitative influence of Rayleigh (*Ra*) and Darcy (*Da*) numbers on thermal transport efficiency and flow characteristics. The surface-averaged Nusselt number (Nu_{av}) demonstrates considerable enhancement with increasing *Ra* from 10^3 to 10^6, particularly at elevated *Da* values, with peak improvement of 65% at $Da = 0.01$. The maximum stream function magnitude (ψ_{max}) exhibits extraordinary amplification with increasing *Ra*, expanding over 500-fold at $Da = 0.01$. Comprehensive entropy production (S_{total}) shows substantial growth with *Ra*, displaying a 2500-fold amplification at $Da = 0.01$. In contrast, the Bejan parameter (*Be*) exhibits an inverse correlation with *Ra*, diminishing by 98.8% at $Da = 0.01$.

While less influential than *Ra*, *Da* exerts a measurable impact, particularly at higher Rayleigh values. For example, at $Ra = 10^6$,

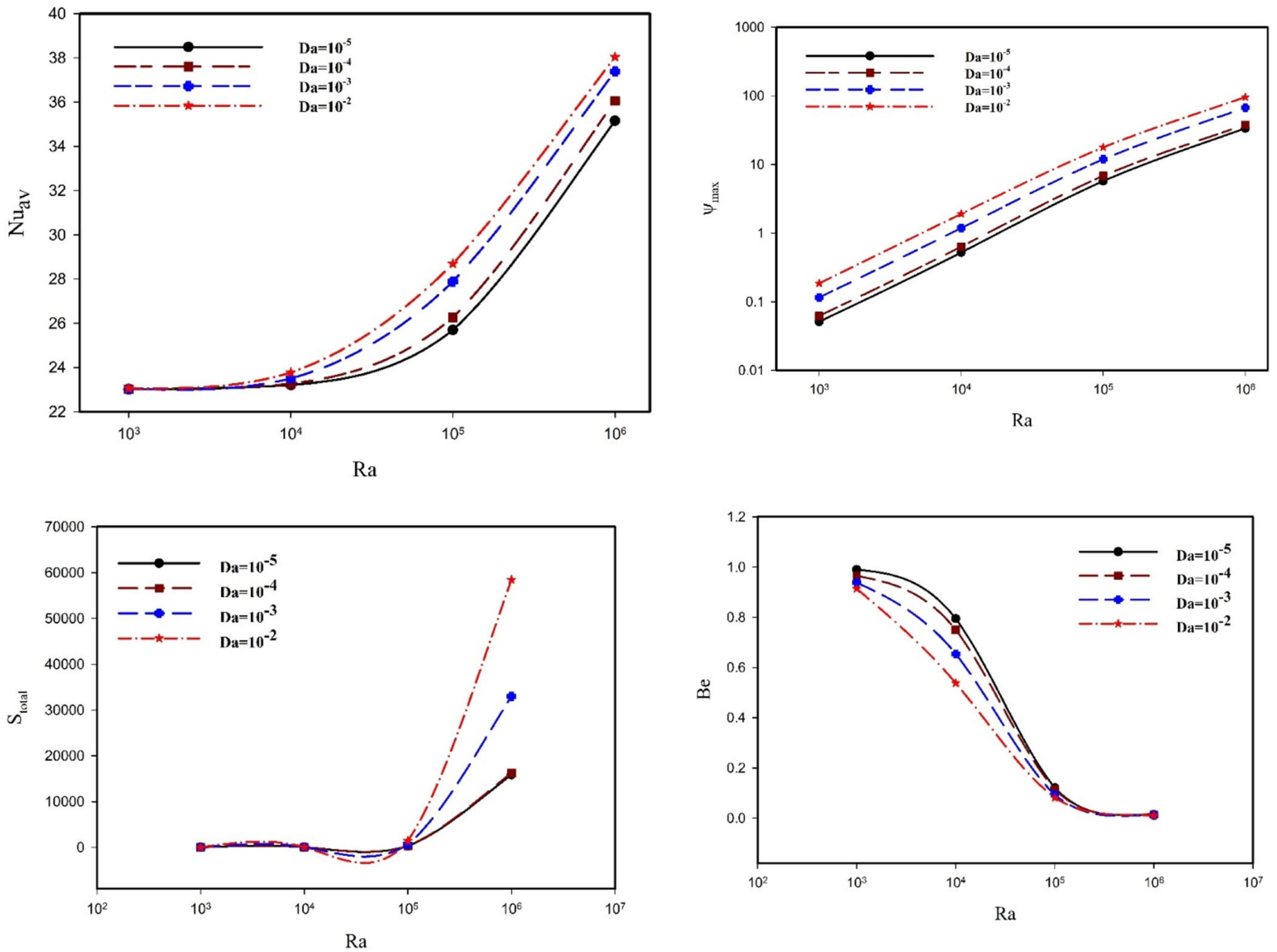

FIGURE 10 | Effect of *Ra* and *Da* on Nu_{av}, ψ, S_{total}, and *Be* for $Ha = 5$, $\gamma = 0$, $\varphi = 0.01$, $\lambda = 1$, and $n_{\text{w}} = 4$.

elevating *Da* from 10^{-5} to 10^{-2} produces an 8.2% enhancement in Nu_{av}, 185% amplification in ψ_{max}, 268% increase in S_{total}, and 27% reduction in *Be*. These correlations indicate improved thermal transport and intensified convective circulation at higher *Ra* and *Da* configurations, accompanied by greater thermodynamic irreversibilities and transition toward viscous dissipation-dominated entropy generation mechanisms.

3.2 | Effect of Magnetic Field

Figure 11 demonstrates the influence of the Hartmann number (*Ha*) and magnetic field orientation angle (γ) on thermal distribution within the triangular enclosure at $Ra = 10^5$. The isothermal contours exhibit notable modifications in heat transport characteristics as these electromagnetic parameters vary. As *Ha* increases from 10 to 80, progressive inhibition of convective thermal transport becomes evident. This suppression manifests through isotherms progressively aligning parallel to the heated lower boundary, particularly at elevated *Ha* values. This phenomenon results from the electromagnetic Lorentz force, which counteracts fluid circulation and diminishes convective currents. At $Ha = 80$, this dampening effect becomes particularly prominent compared with lower *Ha* configurations, with substantially reduced isothermal distortion, indicating a transition toward conduction-dominated thermal transport. Magnetic field orientation angle γ also exerts considerable influence on system behavior. At $\gamma = 0°$ (horizontal field alignment), the electromagnetic force primarily restricts vertical fluid movement, generating more uniform temperature gradients in the vertical direction. The magnetic field's impact on fluid dynamics becomes increasingly complex as γ increases through 45°–90°. Isothermal patterns exhibit moderately increased distortion at $\gamma = 90°$ (vertical field orientation) relative to $\gamma = 0°$, particularly near the inclined boundaries, suggesting that a vertical magnetic field configuration less effectively inhibits convection compared with horizontal orientation. The interactive effects between the Hartmann number and the field orientation angle reveal interesting thermal behavior. At lower *Ha* values, γ variations produce relatively modest changes, as magnetic forces remain insufficient to modify convection patterns substantially. However, orientation effects become more significant at higher *Ha* values, particularly $Ha = 80$. The isotherms for $\gamma = 90°$ show slightly more convective behavior compared with $\gamma = 0°$ at high *Ha*, suggesting that the vertical magnetic field allows some conservation of buoyancy-driven flow.

Figure 12 shows the effect of both *Ha* and γ on the streamlines at the value of (γ) inside the triangular enclosure. A gradual

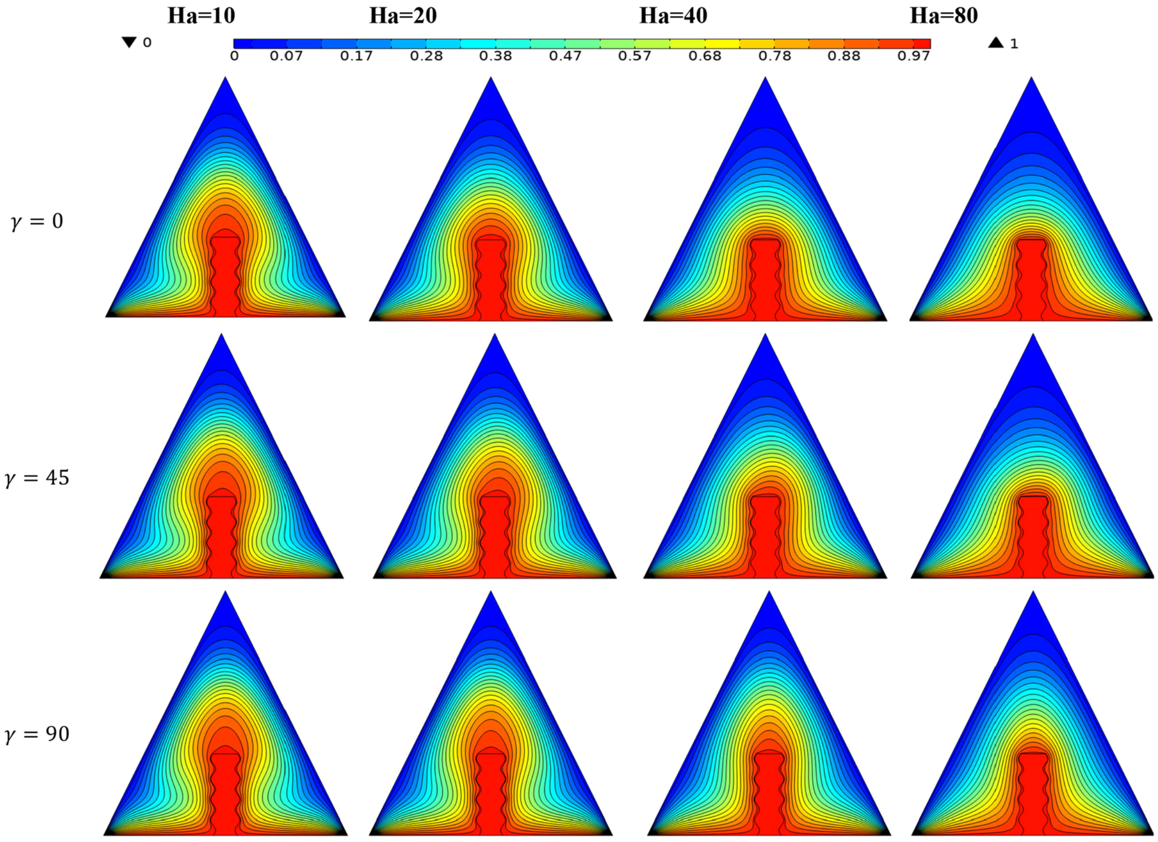

FIGURE 11 | Isotherms contours at different Ha with different values of γ at $Ra = 10^5$, $\varphi = 0.01$, $\lambda = 1$, and $n_w = 4$.

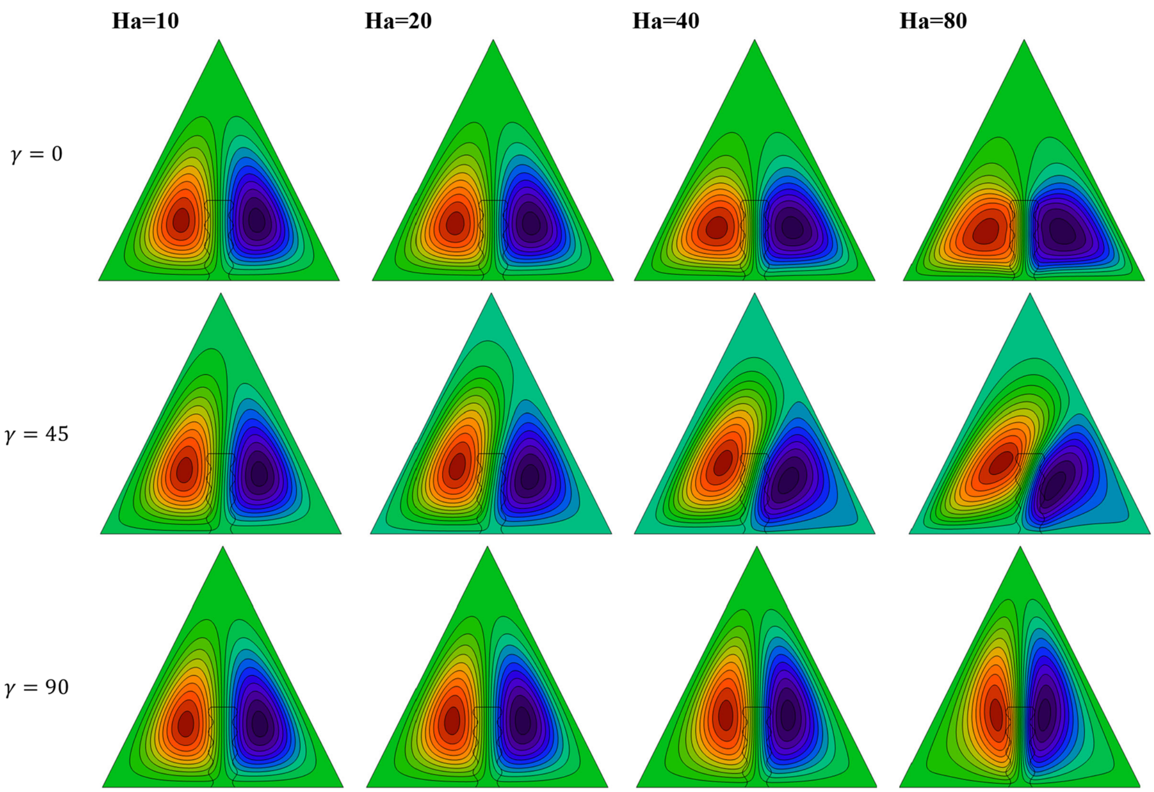

FIGURE 12 | Streamlines contours at different Ha with different values of γ at $Ra = 10^5$, $\varphi = 0.01$, $\lambda = 1$, and $n_w = 4$.

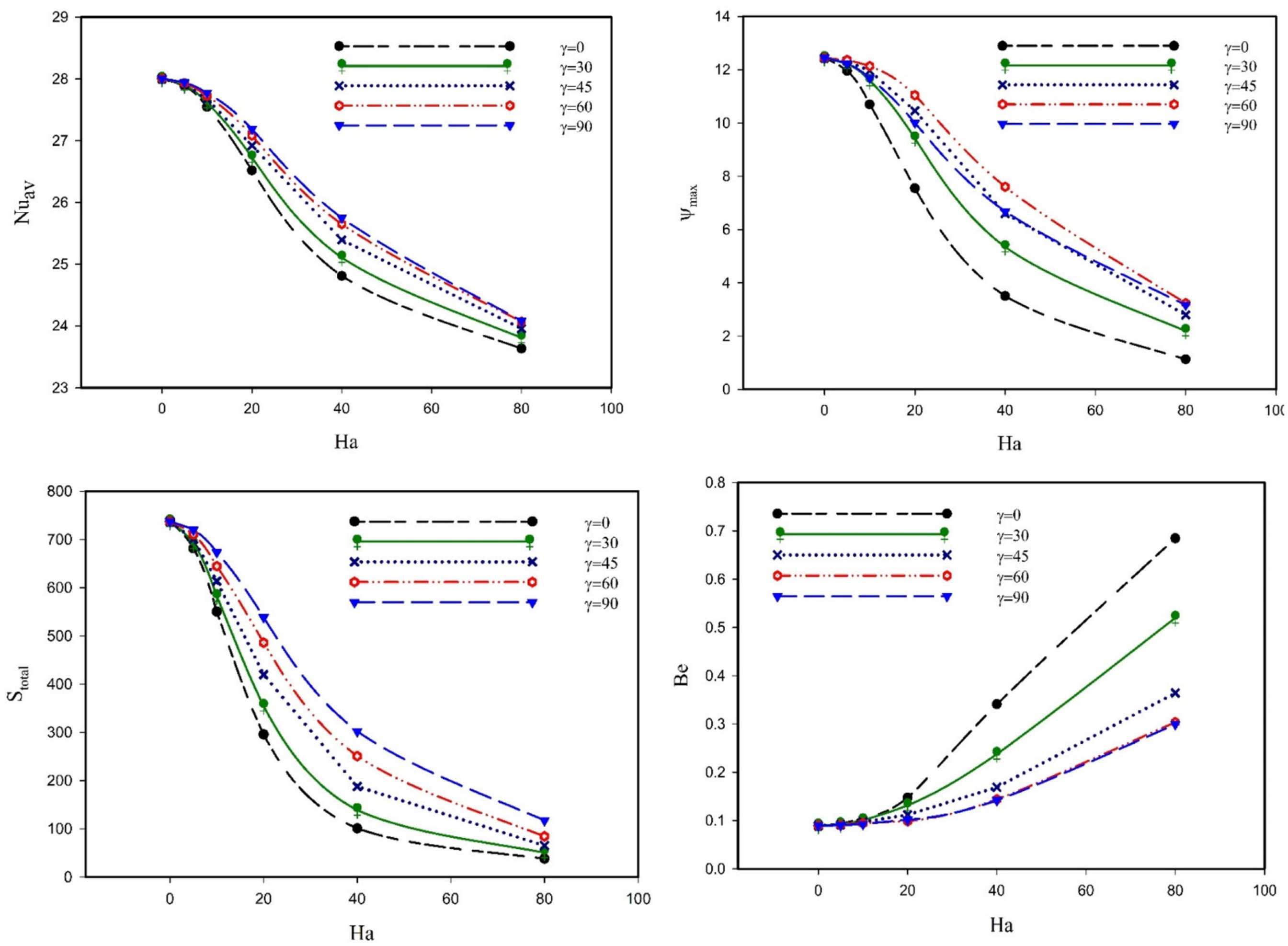

FIGURE 13 | Effect of *Ha* and γ on Nu_{av}, $\psi_{\max}$, S_{total}, and *Be* for $Ra = 10^5$, $\gamma = 0$, $\varphi = 0.01$, $\lambda = 1$, and $n_{\mathrm{w}} = 4$.

weakening of the convective cells is observed with increasing *Ha* from 10 to 80, which indicates a decrease in the intensity of the streamlines. The reason for this weakening is the increase in the Lorentz force, which is opposed to the fluid motion. The convection values are less intense and smaller at the Hartmann number (80) compared with its low value, which shows the extent of the strength of the magnetic field's effect on the fluid flow. Then, the apparent effect of the magnetic field angle is observed. At $\gamma = 0°$ (horizontal field), the magnetic force primarily opposes the vertical fluid motion, resulting in slightly elongated convective cells. As γ increases to 45° and then 90°, the shape and intensity of the convective cells change. At $\gamma = 90°$ (vertical field), the cells become more circular and show slightly stronger circulation compared with the $\gamma = 0°$ case, especially at higher *Ha* values. The interaction between *Ha* and γ reveals complex flow behavior. At lower *Ha*, the effect of γ is less pronounced, as the magnetic force is not strong enough to significantly alter the flow patterns. However, at higher *Ha*, particularly $Ha = 80$, the influence of γ becomes more evident. For $\gamma = 90°$, the convection cells maintain their strength better than at $\gamma = 0°$, indicating that a vertical magnetic field is less effective in suppressing convection than a horizontal one.

Figure 13 represents the effects of the Hartmann number (*Ha*) and magnetic field angle (γ) on key performance metrics. As *Ha* increases from 0 to 80, the average Nusselt number (Nu_{av}) decreases significantly, with the most pronounced effect at $\gamma = 0°$, where Nu_{av} drops by 55.6% from 28.004 to 12.243. The maximum stream function ($\psi_{\max}$) also decreases dramatically with increasing *Ha*, falling by 78.5% from 11.957 to 2.5645 at $\gamma = 0°$. Total entropy generation (S_{total}) shows a complex behavior, initially decreasing with *Ha* up to $Ha = 20$, then increasing for higher *Ha* values. For instance, at $\gamma = 0°$, S_{total} decreases by 59.9% from 737.19 to 295.71 as *Ha* increases from 0 to 20, then rises to 442.85 at $Ha = 80$. The Bejan number (*Be*) generally increases with *Ha*, showing a substantial rise of 665% from 0.089374 to 0.6845 at $\gamma = 0°$ as *Ha* increases from 0 to 80. The effect of γ is less pronounced but still significant, particularly at higher *Ha* values. For example, at $Ha = 80$, increasing γ from 0° to 60° results in a 0.7% increase in Nu_{av}, a 186% increase in $\psi_{\max}$, a 53.7% increase in S_{total}, and a 55.7% decrease in *Be*. These trends suggest that increasing magnetic field strength generally suppresses convection and heat transfer, while changing the field orientation can moderately mitigate these effects, especially at higher *Ha* values.

3.3 | Effect of Nanoparticle Concentration

Figure 14 depicts the effects of nanoparticle volume fraction (φ) and Rayleigh number (*Ra*) on the temperature distribution within the triangular enclosure. The isotherms reveal

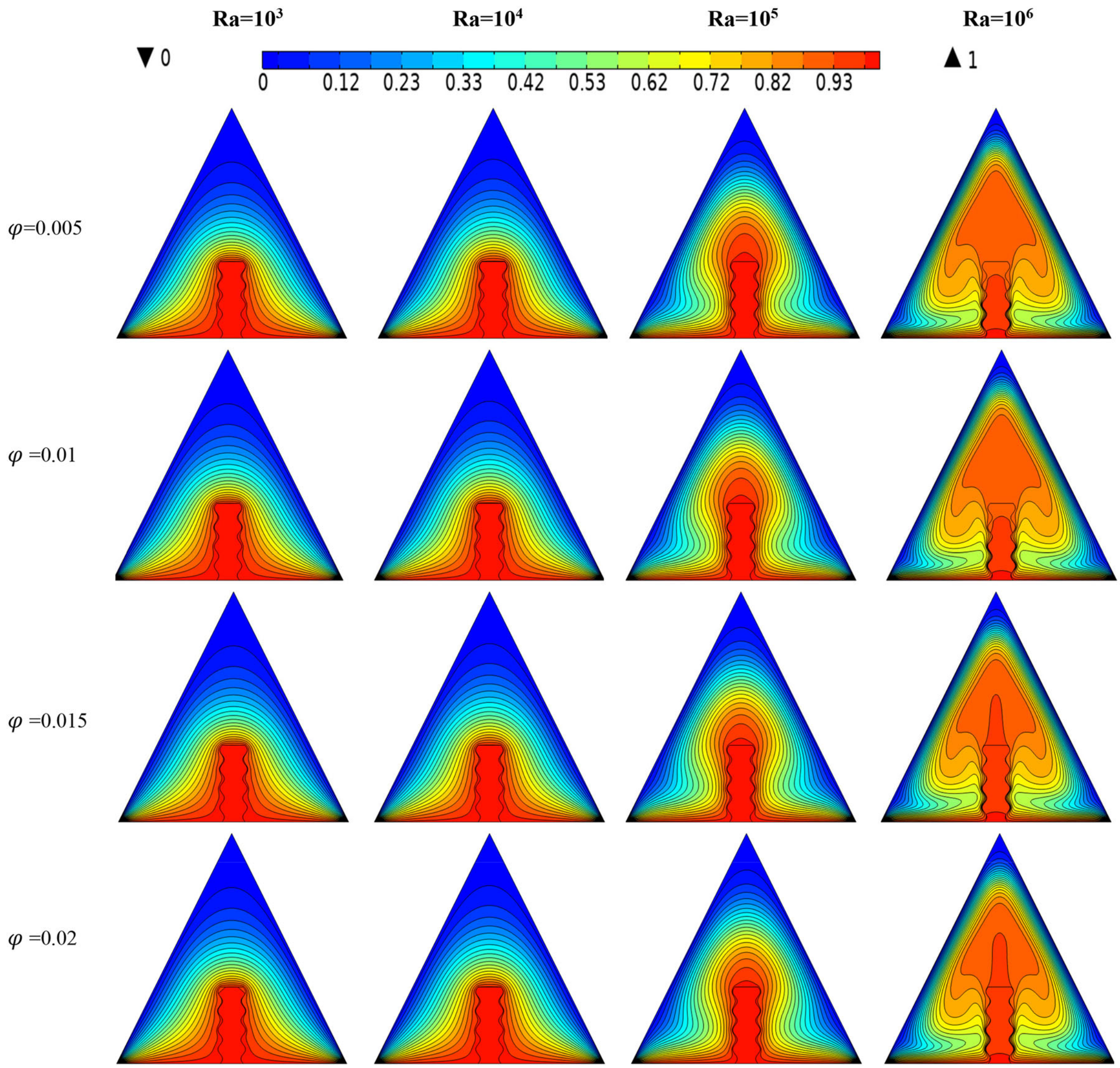

FIGURE 14 | Isotherms contours at different φ with different values of Ra at $\gamma = 0$, $Ha = 5$, $Da = 10^{-3}$, $\lambda = 1$, and $n_w = 4$.

significant changes in heat transfer patterns as these parameters vary. The influence of nanoparticle volume fraction φ is more subtle but still significant. As φ increases from 0.005 to 0.02, we observe slight changes in the isotherm patterns, particularly at higher Ra values. At $Ra = 10^6$, higher φ values lead to more pronounced thermal plumes and thinner boundary layers. This suggests that increasing the nanoparticle concentration enhances heat transfer, likely due to the increased thermal conductivity of the nanofluid.

Figure 15 presents the streamline patterns in the triangular enclosure, illustrating the combined effects of nanoparticle volume fraction (φ) and Rayleigh number (Ra) on the flow structure. The effect of nanoparticle volume fraction φ is more subtle but still noticeable. As φ increases from 0.005 to 0.02 (moving from top to bottom), there is a slight enhancement in the strength of the convection cells, particularly at higher Ra values. This is indicated by the slightly more compact and intense effect of radiation parameters and fin wavy number. Figure 16 demonstrates the effects of nanoparticle volume fraction (φ) and Rayleigh number (Ra) on heat transfer and fluid flow characteristics. As φ increases from 0.005 to 0.02, the (Nu_{av}) shows a moderate increase across all Ra values, with the most significant rise of 11.1% (from 22.143 to 24.601) at $Ra = 10^3$. The impact of Ra on Nu_{av} is more pronounced, with a maximum increase of 66.2% (from 23.036 to 37.391) observed for $\varphi = 0.01$ as Ra rises from 10^3 to 10^6. The maximum stream function (ψ_{max}) decreases slightly with increasing φ, showing a 7.2% reduction (from 68.268 to 63.347) at $Ra = 10^6$ when φ increases from 0.005 to 0.02. Conversely, ψ_{max} increases dramatically with Ra, rising by over 560 times for $\varphi = 0.01$. Total entropy generation (S_{total}) shows a complex behavior, generally increasing with φ at lower Ra values but decreasing at higher Ra. For instance, at $Ra = 10^6$, S_{total} decreases by 3% (from 33178 to 32168) as φ increases from 0.005 to 0.02. The Bejan number (Be) slightly increases with φ but decreases significantly with Ra, dropping by 98.7% (from 0.93837 to 0.011361) for $\varphi = 0.01$ as Ra increases from 10^3 to 10^6. These trends suggest that increasing nanoparticle concentration moderately enhances heat transfer, particularly at lower Ra values, while higher Ra values dominate the system's behavior, significantly intensifying convection and irreversibilities.

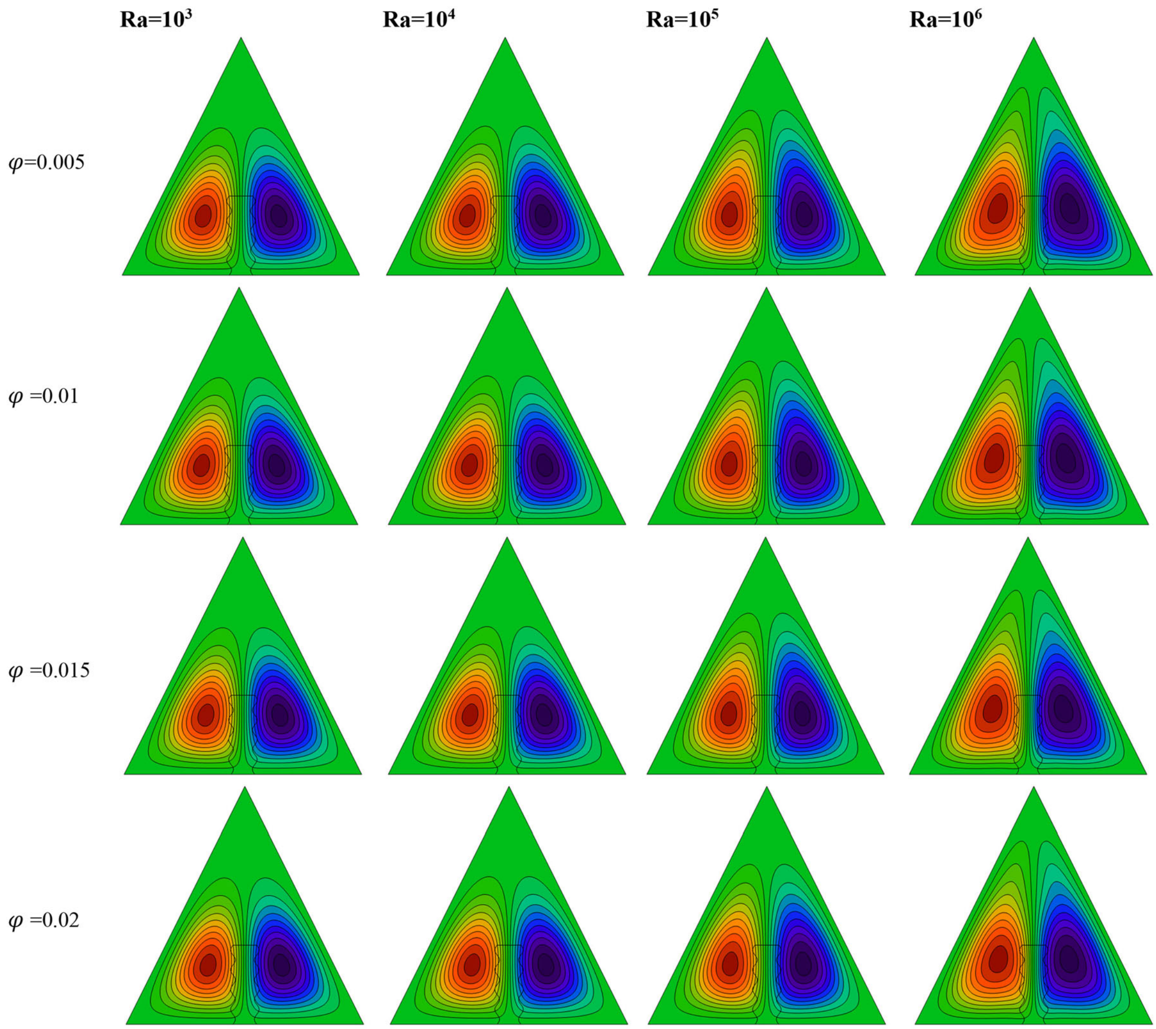

FIGURE 15 | Streamlines contours at different φ with different values of Ra at $\gamma = 0$, $Ha = 5$, $Da = 10^{-3}$, $\lambda = 1$, and $n_w = 4$.

3.4 | Effect of Radiation Parameters and Shape of Fin

Figure 17 shows the effects of heat generation parameter (λ) and fin wavy number (n_w) on the temperature distribution within the triangular enclosure. As λ increases from 1 to 5, we observe a notable increase in the overall temperature within the enclosure. The expansion of the high-temperature region around the fin and the bottom wall evidences this. The isotherms become more closely packed near the inclined walls, indicating steeper temperature gradients. This behavior is due to the increase in λ, which in turn causes an increase in internal heat generation within the fluid, which causes an increase in heat input from the bottom wall. As n_w increases from 0 (straight fin) to 6 (highly wavy fin), which affects the heat transfer value, we see a gradual change in the patterns of the isotherms around the fin. As the waviness increases, the isotherms become more distorted and complex near the fin surface. At higher n_w values, this distortion is particularly noticeable, as the isotherms closely follow the contour of the wavy fin. Two main factors explain this effect. First, increasing λ adds heat to the system, intensifying natural convection and creating a more thermally active environment. Second, the fin waviness increases the surface area for heat transfer and creates local recirculation zones, which can enhance or hinder heat transfer depending on the local flow patterns.

Figure 18 shows the flow patterns inside the triangular enclosure at different heat generation coefficients (λ) and the number of fin wavy numbers (n_w) as indicated by the flow lines. We observe a gradual densification of the convection cells as λ increases from 1 to 5. The densification is due to increased internal heat generation, which enhances the buoyancy-driven flow. At higher λ values, the convection cell cores become more compact and move slightly toward the corners of the container, indicating more vigorous circulation. As n_w increases from 0 (straight fin) to 6 (highly wavy fin), we see slight changes in the shape and structure of the convection cells. With increasing waviness, the streamlines near the fin become more distorted, following the contours of the wavy surface. This distortion is particularly noticeable at higher n_w values, where small secondary vortices begin forming in the wavy fin's troughs.

Figure 19 shows the influence of heat generation (λ) and fin wavy number (n_w) on heat transfer and fluid flow characteristics. As λ increases from 1 to 5, the average Nusselt number (Nu_{av}) slightly decreases across all n_w values, with the most significant reduction of 0.86% (from 27.874 to 27.675) observed

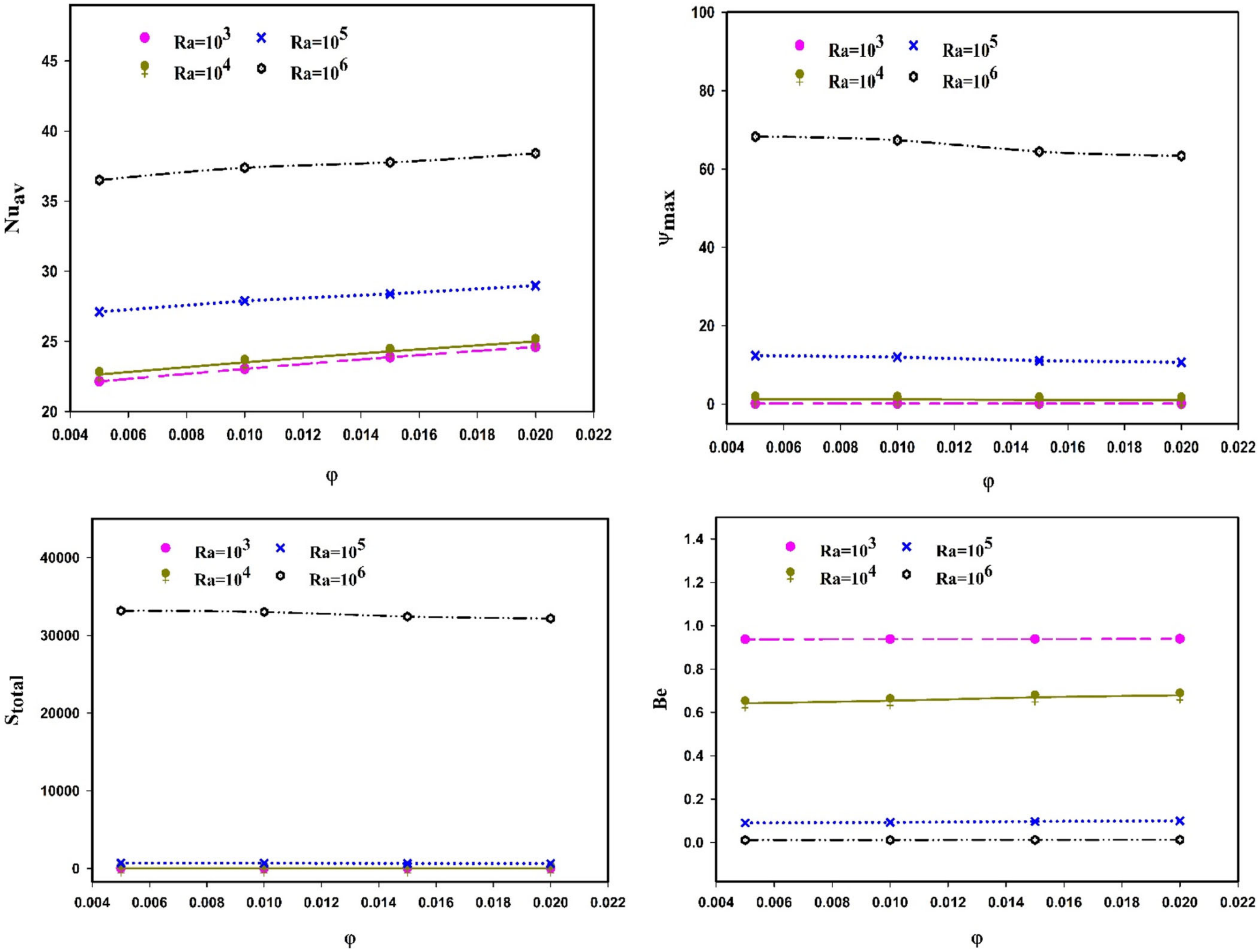

FIGURE 16 | Effect of φ and Ra on Nu_{av}, $\psi_{\max}$, S_{total}, and Be for $Ha=5$, $\gamma=0$, $Da=10^{-3}$, $\lambda=1$, $Rd=1$, and $n_{\mathrm{w}}=4$.

at $n_{\mathrm{w}}=0$. The impact of n_{w} on Nu_{av} is minimal, with variations less than 0.5% across different λ values. The maximum stream function ($\psi_{\max}$) increases moderately with λ, showing a 7.6% rise (from 11.957 to 12.855) at $n_{\mathrm{w}}=4$ when λ increases from 1 to 5. $\psi_{\max}$ also increases slightly with n_{w}, with a maximum increase of 0.51% (from 11.911 to 11.972) at $\lambda=1$. Total entropy generation (S_{total}) shows a significant increase with λ, rising by 11.7% (from 677.48 to 756.91) for $n_{\mathrm{w}}=0$ as λ increases from 1 to 5. The effect of n_{w} on S_{total} is not provided for all cases. The Bejan number (Be) decreases slightly with both λ and n_{w}, with the most considerable reduction of 0.65% (from 0.092673 to 0.092069) occurring when λ increases from 1 to 5 at $n_{\mathrm{w}}=6$. These trends suggest that increasing heat generation moderately enhances fluid circulation and entropy generation while slightly reducing overall heat transfer efficiency. The waviness of the fin has a minor impact on these parameters, with slight improvements in fluid circulation but marginal reductions in heat transfer and Bejan number as waviness increases.

Figure 20 explains the combined effects of the radiation parameter (Rd) and Rayleigh number (Ra) on the temperature distribution within the triangular enclosure, as represented by isotherms. As Ra increases from 10^3 to 10^6, we observe a significant transformation in the isotherm patterns, indicating a shift from conduction-dominated to convection-dominated heat transfer. At lower Ra values (10^3 and 10^4), the isotherms are nearly parallel to the heated bottom wall, suggesting conduction is the primary heat transfer mechanism. The isothermal lines become very distorted, with thermal columns and boundary layers forming as Ra increases to 10^5 and especially at 10^6, indicating strong convection currents. We observe a gradual smoothing of the temperature gradients as Rd increases from 1 to 5, especially at higher Ra values. This is evident by the slight spreading of the isothermal lines and their reduced concentration near the walls. The thermal columns become less sharp and more diffuse, and this effect is most pronounced at $Ra=10^6$ and as Rd increases. The results indicate that both convection (controlled by Ra) and radiation (influenced by Rd) play a decisive role in shaping the temperature distribution inside the enclosure. At high-Ra values, convection creates strong thermal columns and boundary layers, while increased radiation tends to smooth these features, resulting in a more uniform temperature distribution.

Figure 21 shows the combined effects of the radiation parameter (Rd) and Rayleigh number (Ra) on the flow patterns within the triangular enclosure, as represented by streamlines. The impact of the radiation parameter Rd is more subtle but still notable. As Rd increases from 1 to 5, we observe slight changes in the structure and intensity of the convection cells. The

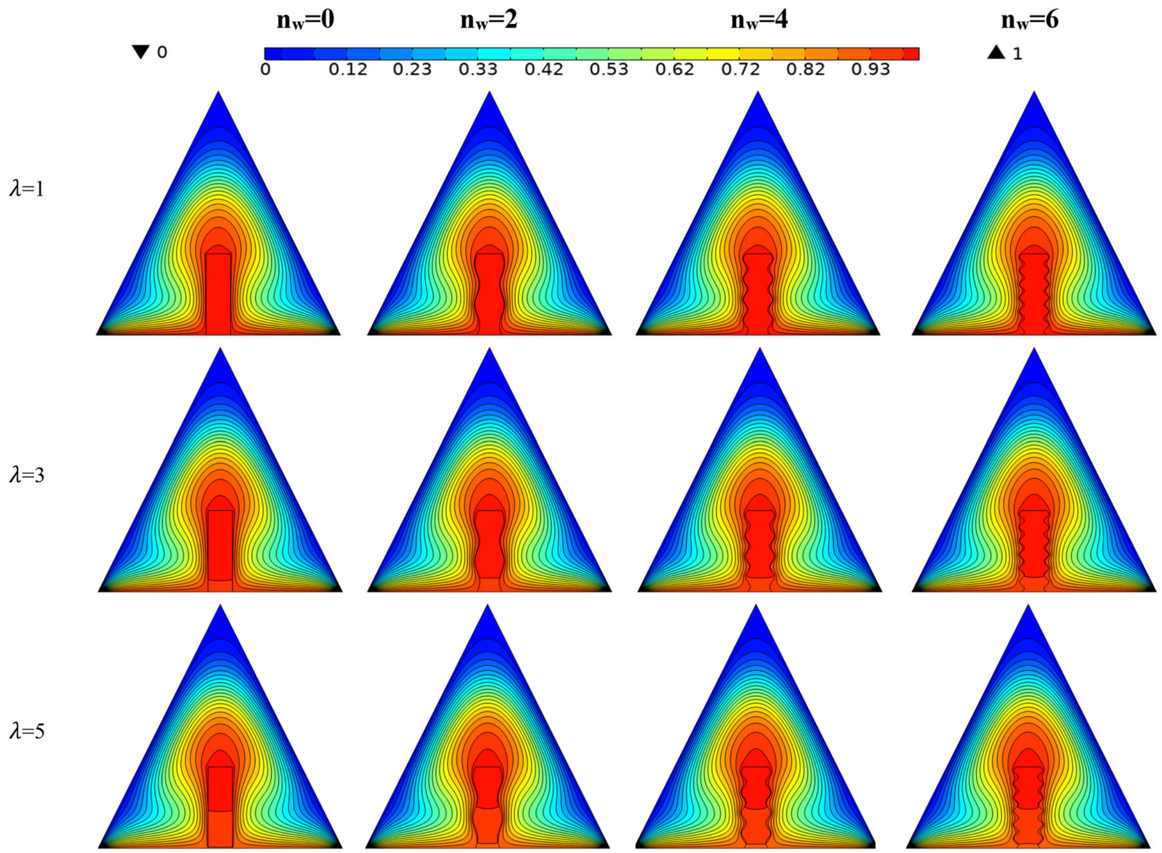

FIGURE 17 | Isotherms contours at different λ with different values of n_w at $Ra = 10^5$, $\gamma = 0$, $Ha = 5$, $Da = 10^{-3}$, $\varphi = 0.01$, and $Rd = 1$.

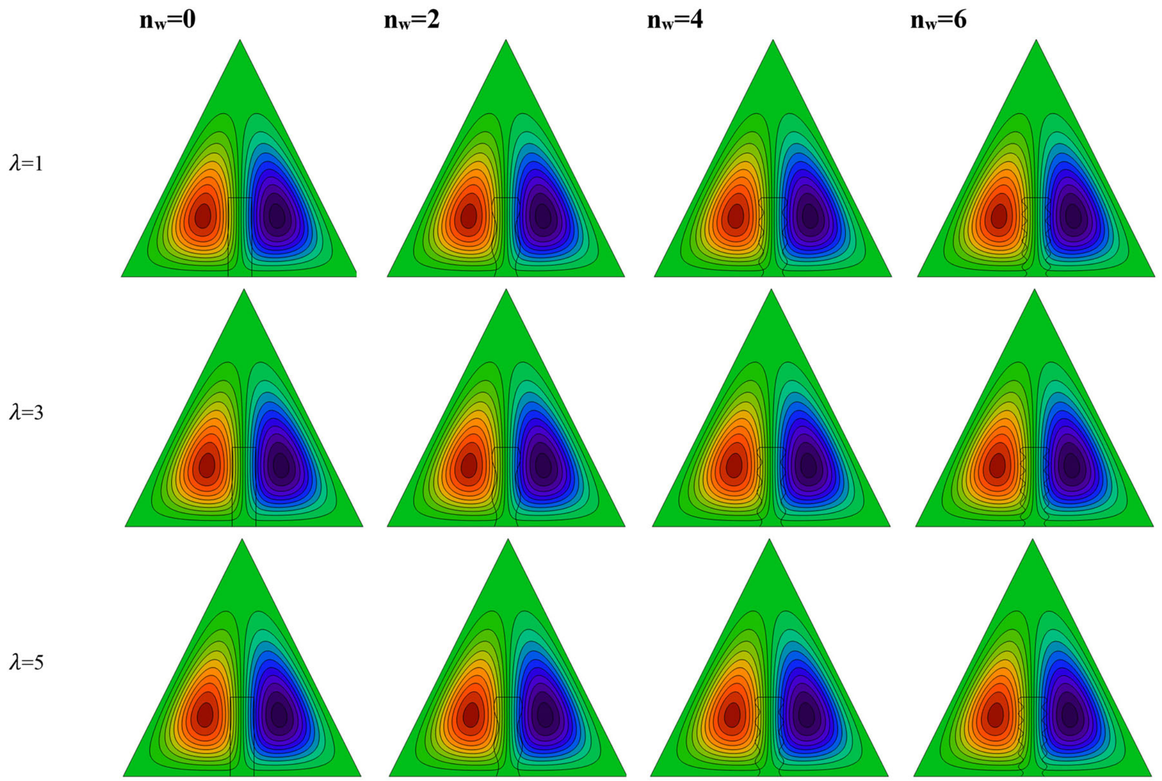

FIGURE 18 | Streamlines contours at different λ with different values of n_w at $Ra = 10^5$, $\gamma = 0$, $Ha = 5$, $Da = 10^{-3}$, $\varphi = 0.01$, and $Rd = 1$.

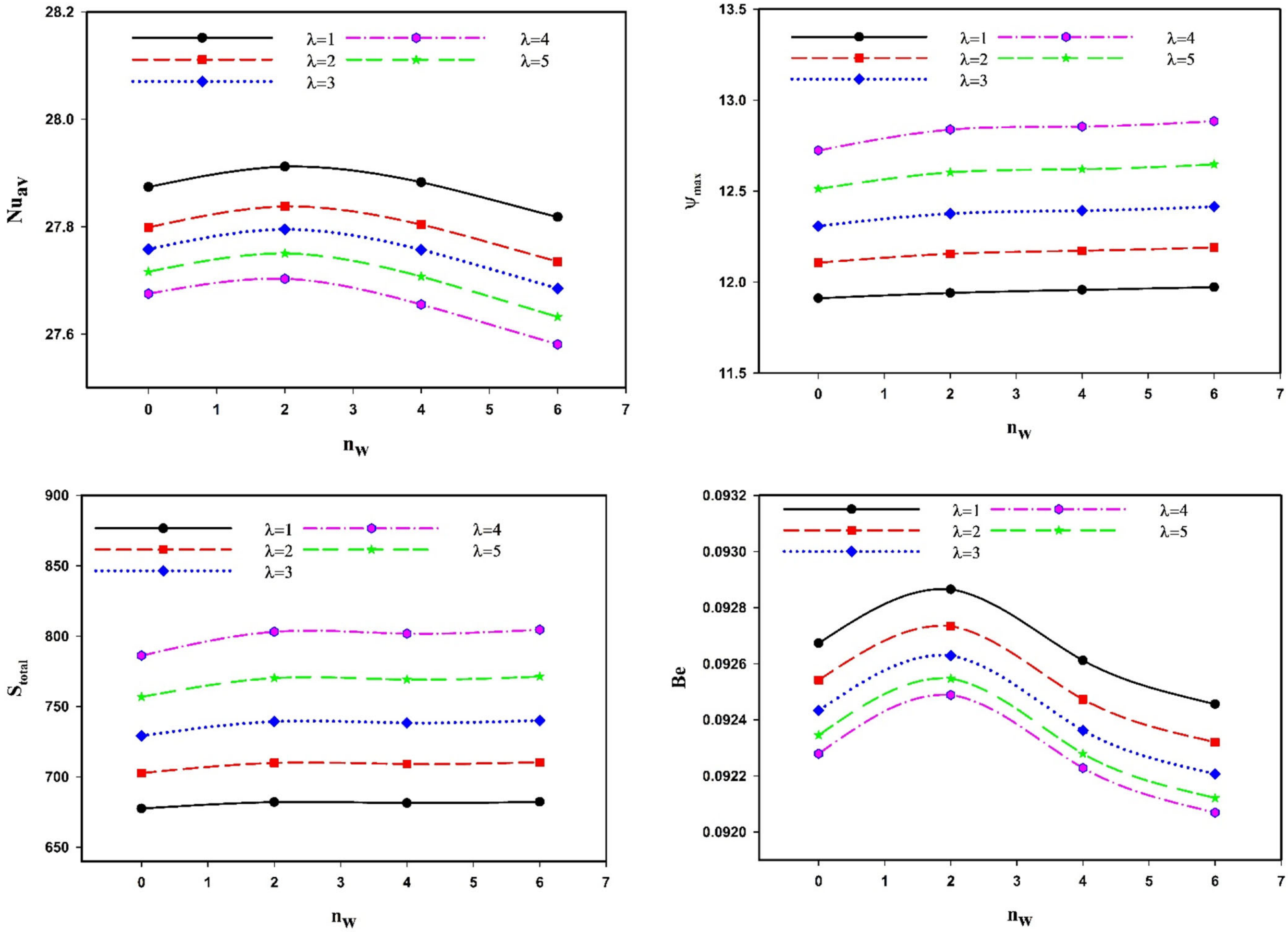

FIGURE 19 | Effect of λ and n_w on Nu_{av}, ψ_{max}, S_{total}, and Be for at $Ra = 10^5$, $\gamma = 0$, $Ha = 5$, $Da = 10^{-3}$, $\varphi = 0.01$, and $Rd = 1$.

streamlines appear slightly spread out at higher Rd values, particularly at higher Ra values. This suggests that increased radiation tends to moderate the intensity of the convection cells. The interaction between Ra and Rd reveals interesting flow behavior. At lower Ra values, the effect of increasing Rd is minimal, as weak buoyancy forces primarily drive the flow. However, at higher Ra values, especially at 10^6, the influence of Rd becomes more apparent. The convection cells remain strong, but their structure is slightly modified, with a tendency toward more uniform circulation throughout the enclosure.

Figure 22 illustrates the effects of the radiation parameter (Rd) and Rayleigh number (Ra) on key heat transfer and fluid flow characteristics. The (Nu_{av}) rises significantly with Rd and Ra. As Rd increases from 1 to 5, Nu_{av} shows a substantial rise across all Ra values, with the most pronounced increase at higher Ra. For $Ra = 10^6$, Nu_{av} nearly triples as Rd increases from 1 to 5. The effect of Ra on Nu_{av} is also significant, with higher Ra values consistently yielding higher Nu_{av} across all Rd values. The maximum stream function (ψ_{max}) strongly depends on Ra but is less affected by Rd. As Ra increases from 10^3 to 10^6, ψ_{max} increases dramatically, indicating much stronger convection at higher Ra. The effect of Rd on ψ_{max} is relatively minor, showing only a slight increase as Rd increases, particularly at higher Ra values. Total entropy generation (S_{total}) exhibits a complex behavior. It increases substantially with Ra, with the highest values observed at $Ra = 10^6$. The effect of Rd on S_{total} is most pronounced at high Ra, where S_{total} shows a moderate increase with increasing Rd. For lower Ra values, the impact of Rd on S_{total} is minimal. The Bejan number (Be) decreases significantly with increasing Ra, indicating that fluid friction becomes the dominant source of irreversibility at higher Ra values. Be shows a slight variation with Rd, suggesting that the radiation parameter minimally impacts heat and friction to entropy generation. These trends indicate that radiation and natural convection play crucial roles in heat transfer, with their effects being most significant at higher Rayleigh numbers. The increase in Nu_{av} with Rd indicates that the radiation enhances the overall heat transfer, especially in strongly convective regimes. The minimal impact of Rd on ψ_{max} and Be implies that radiation primarily affects heat transfer rather than fluid flow patterns or the nature of irreversibilities in the system.

4 | Conclusions

On the basis of our comprehensive analysis of the various parameters affecting heat transfer and fluid flow in the triangular enclosure with a porous fin, we can draw the following conclusions:

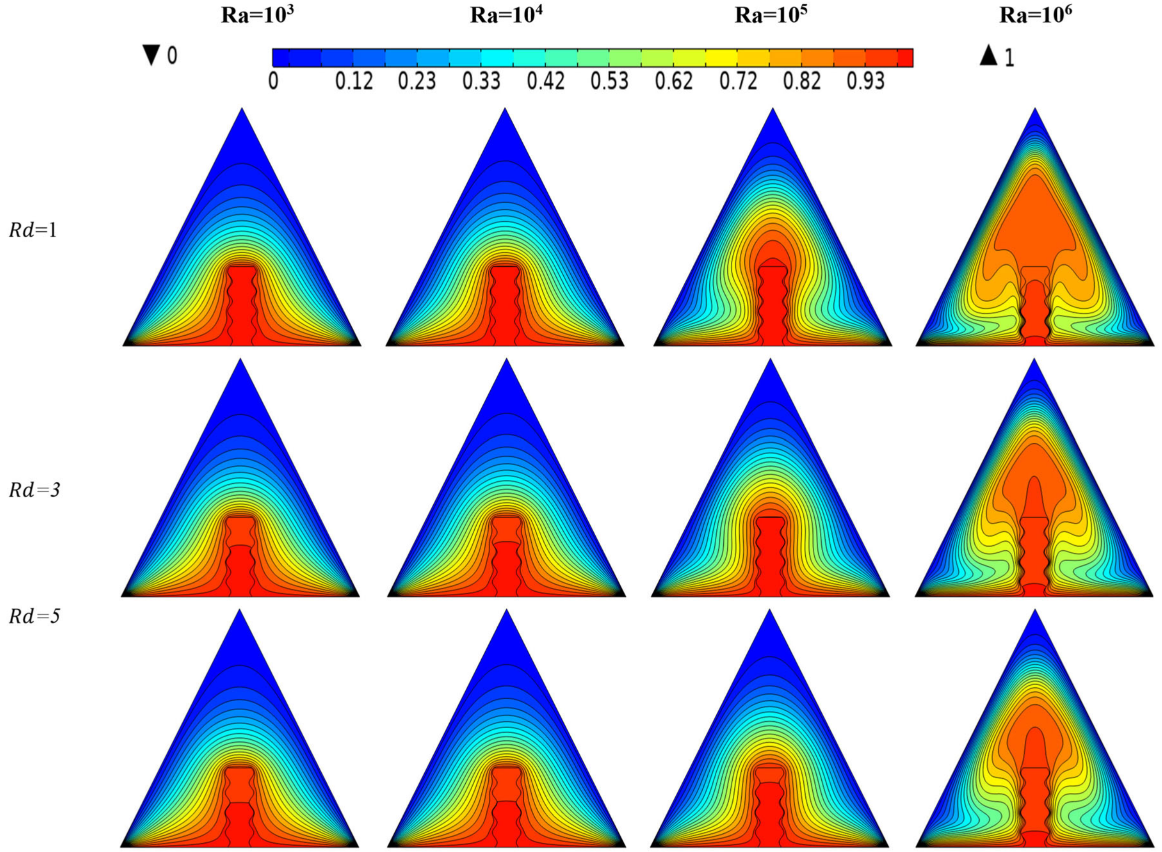

FIGURE 20 | Isotherms contours at different Rd with different values of Ra at $n_w = 4$, $\gamma = 0$, $Ha = 5$, $Da = 10^{-3}$, $\varphi = 0.01$, and $\lambda = 1$.

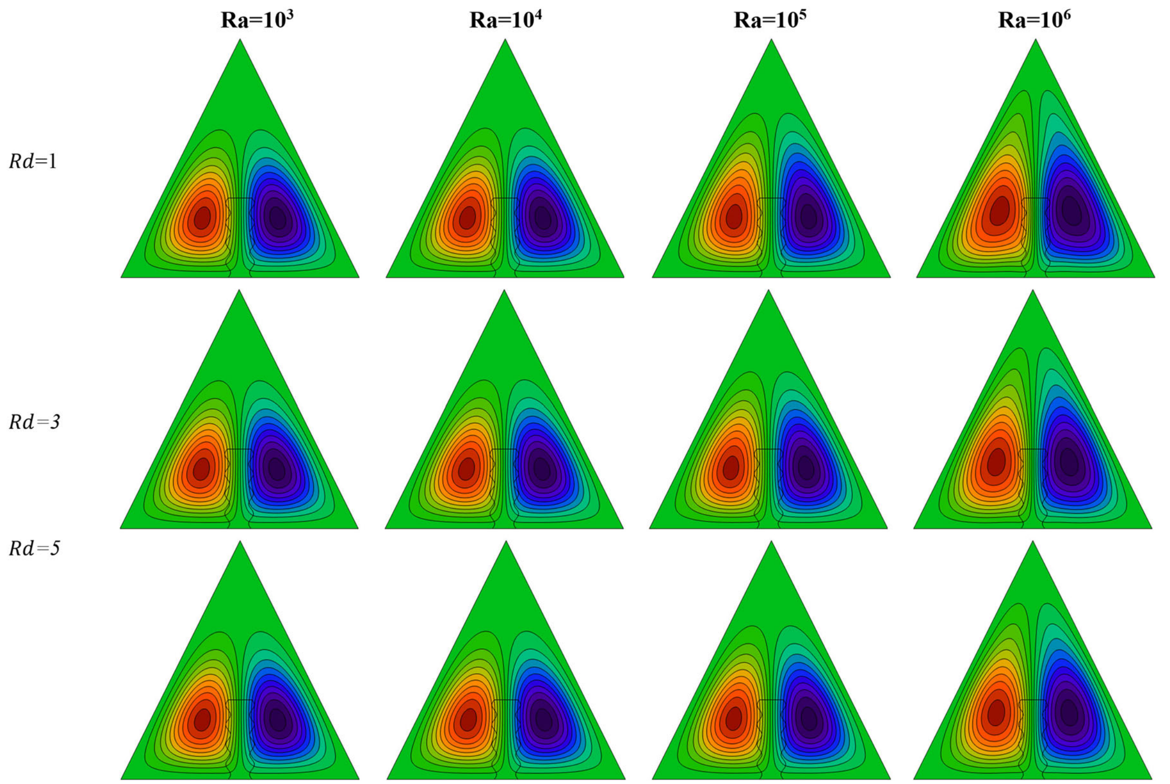

FIGURE 21 | Streamlines contours at different Rd with different values of Ra at $n_w = 4$, $\gamma = 0$, $Ha = 5$, $Da = 10^{-3}$, $\varphi = 0.01$, and $\lambda = 1$.

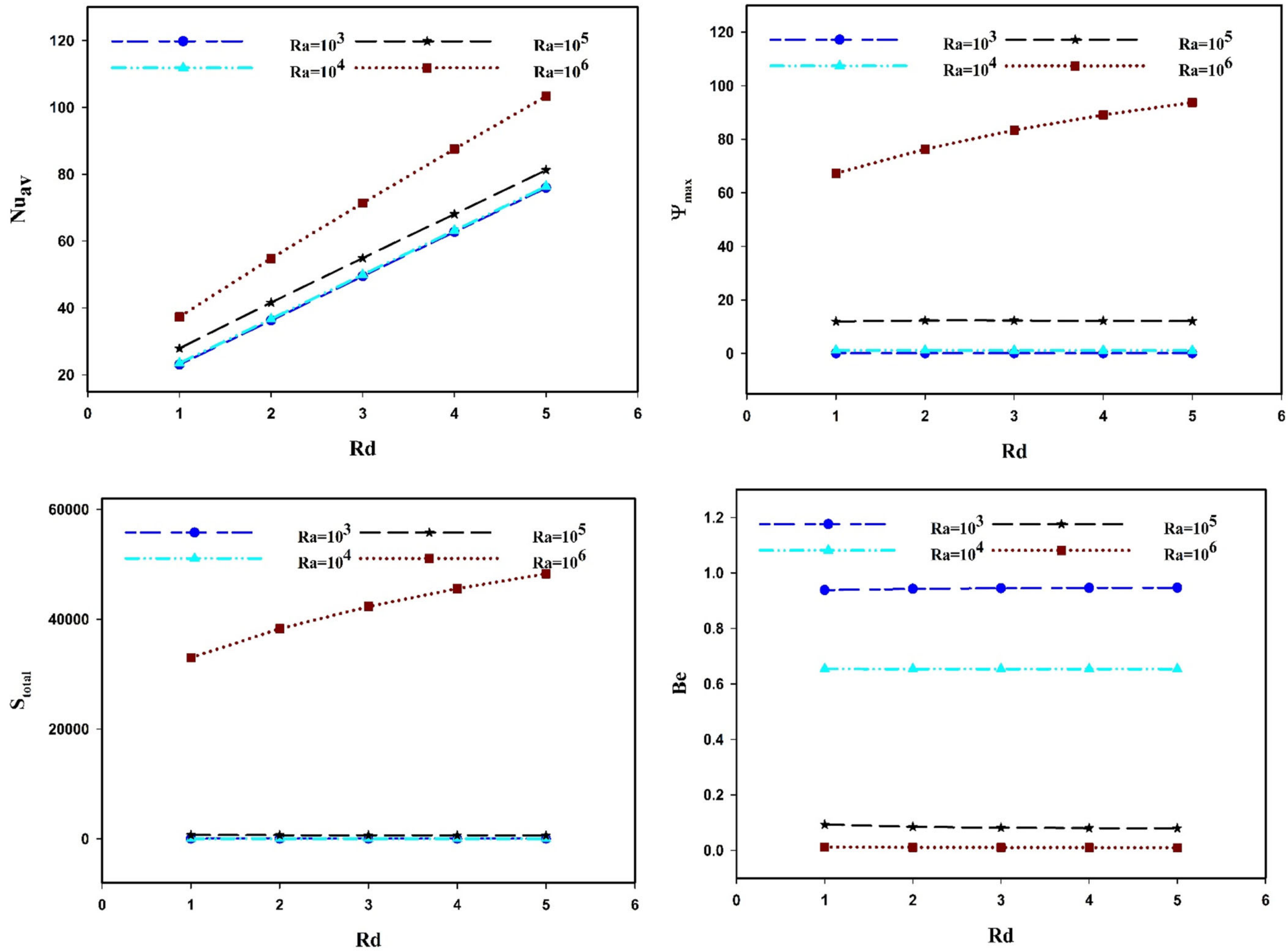

FIGURE 22 | Effect of Rd and Ra on Nu_{av}, $\psi_{\max}$, S_{total}, and Be for at $n_{\mathrm{w}} = 4$, $\gamma = 0$, $Ha = 5$, $Da = 10^{-3}$, $\varphi = 0.01$, and $\lambda = 1$.

1. The Rayleigh number (Ra) significantly impacts heat transfer and fluid flow characteristics. Increasing Ra from 10^3 to 10^6 led to a 65% increase in the average Nusselt number (Nu_{av}) and over 500-fold increase in maximum stream function ($\psi_{\max}$), indicating substantially enhanced convection and heat transfer at higher Ra values.
2. The Darcy number (Da) shows a moderate effect, with an 8.2% rise in Nu_{av} as Da increased from 10^{-5} to 10^{-2}. This suggests that increasing the permeability of the porous medium can modestly improve heat transfer performance.
3. Magnetic field strength, represented by the Hartmann number (Ha), demonstrates a suppressive effect on heat transfer. Nu_{av} decreased by 55.6% as Ha increased from 0 to 80, indicating that strong magnetic fields can significantly inhibit convective heat transfer.
4. The magnetic field angle (γ) shows a minor but notable influence, particularly at higher Ha values. Changing γ from 0° to 60° at $Ha = 80$ resulted in a 0.7% increase in Nu_{av} and a 186% increase in $\psi_{\max}$, suggesting that the orientation of the magnetic field can be used to fine-tune heat transfer characteristics.
5. Nanoparticle addition provides modest benefits to heat transfer. Increasing the nanoparticle volume fraction (φ) from 0.005 to 0.02 led to an 11.1% increase in Nu_{av} at $Ra = 10^3$, indicating that nanofluid use can enhance heat transfer, particularly at lower Ra values. This effect is more significant under low-Ra conditions due to the dominance of thermal conductivity enhancement over viscosity increase. At low Ra, convection is weak, making conductive heat transfer through enhanced thermal conductivity the primary mechanism. Additionally, reduced Brownian motion at lower temperatures allows nanoparticles to maintain stable thermal pathways, maximizing their conductivity benefits.
6. The heat generation parameter (λ) and fin wavy number (n_{w}) show relatively minor effects on overall heat transfer performance. Increasing λ from 1 to 5 led to a slight decrease in Nu_{av} (0.86% at $n_{\mathrm{w}} = 0$) but increased $\psi_{\max}$ by 7.6%, suggesting a complex interaction between heat generation and fluid flow.
7. The radiation parameter (Rd) significantly influences heat transfer, especially at higher Ra values. Nu_{av} nearly tripled at $Ra = 10^6$ as Rd increased from 1 to 5, highlighting the importance of considering radiative heat transfer in high-temperature or high-Ra applications.
8. Entropy generation analysis reveals that fluid friction becomes the dominant source of irreversibility at higher

Ra values, as evidenced by the significant decrease in the Bejan number (*Be*) with increasing *Ra*. From a second law of thermodynamics perspective, the Bejan number represents the ratio of heat transfer irreversibility to total entropy generation, providing crucial insights for engineering optimization. At low-*Ra* values ($Be \approx 0.94$), heat transfer irreversibilities dominate, suggesting that optimization efforts should focus on minimizing thermal gradients through enhanced thermal conductivity or improved heat exchanger design. Conversely, at high-*Ra* values ($Be \approx 0.01$), fluid friction irreversibilities become predominant, indicating that engineering optimization should prioritize reducing viscous losses through streamlined geometries, optimized flow paths, or reduced fluid viscosity. This analysis provides a clear roadmap for system designers: in conduction-dominated regimes, enhance thermal properties; in convection-dominated regimes, minimize flow resistance and optimize fluid dynamics.

Future Research Directions:

1. Experimental validation of the numerical predictions presented in this study to verify the accuracy of the theoretical models and provide benchmark data for further computational studies.
2. Investigation of time-dependent and transient effects in hybrid nanofluid systems under varying electromagnetic conditions to understand dynamic behavior and system response times.
3. Extension of the current model to three-dimensional geometries and more complex fin configurations to enhance practical applicability in real-world thermal management systems.
4. Development of artificial intelligence and machine learning algorithms for optimizing parameter combinations to achieve maximum heat transfer efficiency while minimizing entropy generation.
5. Exploration of different hybrid nanofluid combinations and their molecular-level interactions to identify superior thermal enhancement materials.
6. Investigation of the economic and environmental impacts of implementing such systems in industrial applications to assess their practical viability and sustainability.

These findings provide valuable insights for optimizing thermal management strategies in applications involving porous media, nanofluids, and magnetic fields, contributing to the advancement of heat transfer enhancement technologies in various engineering applications.

Acknowledgments

The authors thank Qatar National Library for providing open access funding. The authors are thankful to the Deanship of Scientific Research at the University of Bisha for supporting this study through the Fast-Track Research Support Program.

Conflicts of Interest

The authors declare no conflicts of interest.

References

1. H. Singh and P. C. Eames, "A Review of Natural Convective Heat Transfer Correlations in Rectangular Cross-Section Cavities and Their Potential Applications to Compound Parabolic Concentrating (CPC) Solar Collector Cavities," *Applied Thermal Engineering* 31, no. 14–15 (2011): 2186–2196, https://doi.org/10.1016/j.applthermaleng.2011.05.032.

2. A. A. Alwan and A. M. Hassan, "Experimental Study on Optimizing Photovoltaic Panel Efficiency: Harnessing Paraffin Wax Phase Change for Temperature Reduction," *Arabian Journal for Science and Engineering* 49 (2024): 1–14, https://doi.org/10.1007/s13369-023-08581-3.

3. M. S. Kassim, A. Oleiwi, D. S. Khudhur, and L. J. Habeeb, "Three Dimensional Study of Baffles Effect on Heat Transfer in Shell and Tube Heat Exchanger," *Journal of Mechanical Engineering Research and Developments* 43, no. 5 (2020): 332–345.

4. S. Singh and M. A. R. Sharif, "Mixed Convective Cooling of a Rectangular Cavity With Inlet and Exit Openings on Differentially Heated Side Walls," *Numerical Heat Transfer, Part A: Applications* 44, no. 3 (2003): 233–253, https://doi.org/10.1080/716100509.

5. M. Bilal, A. Alameer, H. Ahmad, H. A. El-Wahed khalifa, A. A. Shaaban, and Y. Khan, "Numerical Study of an Electrically Conducting Nanofluid Flow Past a Vertical Stretching Riga Plate," *Journal of Radiation Research and Applied Sciences* 17, no. 4 (2024): 101195.

6. A. M. Hassan, M. A. Alomari, Q. H. Al-Salami, F. Alqurashi, M. A. Flayyih, and A. M. Sadeq, "Numerical Analysis of MHD Combined Convection for Enhanced CPU Cooling in NEPCM-Filled a Trapezoidal Cavity," *International Communications in Heat and Mass Transfer* 159 (2024): 108343, https://doi.org/10.1016/j.icheatmasstransfer.2024.108343.

7. A. M. Hassan, M. A. Alomari, Q. H. Al-Salami, F. Q. A. Alyousuf, F. Alqurashi, and M. A. Flayyih, "Active Cooling of Hot Integrated Circuits Using a Rotating Cylinder and NEPCM–Water Mixture: Numerical Analysis of the Impact of Phase Change and Magnetohydrodynamics on Double-Diffusive Mixed Convection," *International Communications in Heat and Mass Transfer* 159 (2024): 107987, https://doi.org/10.1016/j.icheatmasstransfer.2024.107987.

8. A. M. Hassan, M. A. Alomari, Q. H. Al-Salami, F. A. Alyousuf, F. Alqurashi, and M. A. Flayyih, "Numerical Analysis of Hydrothermal Performance and Entropy Generation in an Active Cooling System: A Case Study With NEPCM, Double-Diffusive Mixed-Convection and MHD," *Case Studies in Thermal Engineering* 61 (2024): 105064, https://doi.org/10.1016/j.csite.2024.105064.

9. T. Hai, I. Omar, A. a. Alizadeh, et al., "Optimization of Nano-Finned Enclosure-Shaped Latent Heat Thermal Energy Storage Units Using CFD, RSM, and Enhanced Hill Climbing Algorithm," *Scientific Reports* 151 (2025): 12486.

10. A. A. Ali, D. Alfarge, F. l. Rashid, A. A. Ugla, A. Kareem, and H. I. Mohammed, "Improving Photovoltaic Panels by Utilizing Ground-Coupled Heat Exchangers: Insights and Technological Advances," *Geothermics* 130 (2025): 103335.

11. O. Mahian, A. Kianifar, S. A. Kalogirou, I. Pop, and S. Wongwises, "A Review of the Applications of Nanofluids in Solar Energy," *International Journal of Heat and Mass Transfer* 57, no. 2 (2013): 582–594, https://doi.org/10.1016/j.ijheatmasstransfer.2012.10.037.

12. M. A. Said, H. S. S. Aljibori, A. M. Abed, et al., "Innovative Pipe Profile Configurations for Fast Charging of Phase Change Material in Compact Thermal Storage Systems for Building Heating Applications," *Case Studies in Thermal Engineering* 69 (2025): 106036.

13. K. Thirumalaisamy, R. Sivaraj, and A. S. Reddy, "Fluid Flow and Heat Transfer Analysis of a Ternary Aqueous Fe_3O_4 + MWCNT + Cu/H_2O Magnetic Nanofluid in an Inclined Rectangular Porous Cavity," *Journal of Magnetism and Magnetic Materials* 589 (2024): 171503, https://doi.org/10.1016/j.jmmm.2023.171503.

14. S. O. Giwa, M. Sharifpur, J. P. Meyer, R. T. Taziwa, and N. A. Shah, "Synergetic Effect of Magnetic Field Location, Strength and Orientation on Heat Transfer Characteristics of Brine-Based Hybrid Nanofluid in Rectangular Confinement," *Journal of Magnetism and Magnetic Materials* 590 (2024): 171642, https://doi.org/10.1016/j.jmmm.2023.171642.

15. A. M. Hassan, M. A. Alomari, Q. H. Al-Salami, F. Q. A. Alyousuf, F. Alqurashi, and M. A. Flayyih, "Numerical Analysis of Free Convection Under the Influence of Radiation and Inclined MHD in a Triangular Cavity Filled With Hybrid Nanofluid and a Porous Fin," *International Journal of Thermofluids* 24 (2024): 100843, https://doi.org/10.1016/j.ijft.2024.100843.

16. K. Hosseinzadeh, M. A. Erfani Moghaddam, S. Nateghi, M. Behshad Shafii, and D. D. Ganji, "Radiation and Convection Heat Transfer Optimization With MHD Analysis of a Hybrid Nanofluid Within a Wavy Porous Enclosure," *Journal of Magnetism and Magnetic Materials* 566 (2023): 170328, https://doi.org/10.1016/j.jmmm.2022.170328.

17. M. A. Sheremet, H. F. Oztop, and I. Pop, "MHD Natural Convection in an Inclined Wavy Cavity With Corner Heater Filled With a Nanofluid," *Journal of Magnetism and Magnetic Materials* 416 (2016): 37–47, https://doi.org/10.1016/j.jmmm.2016.04.061.

18. R. H. Hameed, A. M. Hassan, R. A. Hussein, A. Oliwie, and N. H. Hamza, "CFD Analysis of Mixed Convection and Entropy Generation in Vented Curved Cavity Under the Radiation Effects," *European Physical Journal Plus* 139, no. 8 (2024): 756, https://doi.org/10.1140/epjp/s13360-024-05546-9.

19. A. M. Hassan, M. A. Alomari, A. Alajmi, A. M. Sadeq, F. Alqurashi, and M. A. Flayyih, "Numerical Analysis of Nano-Encapsulated PCM Magnetohydrodynamics Double-Diffusive Convection and Entropy Generation in Vertical Enclosures With Porous Layer," *Results in Engineering* 24 (2024): 103579, https://doi.org/10.1016/j.rineng.2024.103579.

20. M. F. Al-Dawody, A. M. Hassan, A. Abdulkadhim, et al., "Magnetic Field Effects on Double-Diffusive Mixed Convection and Entropy Generation in a CAM-Shaped Enclosure," *International Communications in Heat and Mass Transfer* 159 (2024): 108166.

21. H. F. Oztop and E. Abu-Nada, "Numerical Study of Natural Convection in Partially Heated Rectangular Enclosures Filled With Nanofluids," *International Journal of Heat and Fluid Flow* 29, no. 5 (2008): 1326–1336, https://doi.org/10.1016/j.ijheatfluidflow.2008.04.009.

22. M. I. Ur Rehman, H. Chen, F. Z. Duraihem, M. Hussien, A. Hamid, and H. J. Qi, "Darcy–Forchheimer Aspect on Unsteady Bioconvection Flow of Reiner–Philippoff Nanofluid Along a Wedge With Swimming Microorganisms and Arrhenius Activation Energy," *Numerical Heat Transfer, Part A: Applications* (2024): 1–19.

23. M. I. U. Rehman, H. Chen, A. Hamid, and H. J. Qi, "Numerical Analysis of Unsteady Non-Linear Mixed Convection Flow of Reiner–Philippoff Nanofluid Along Falkner–Skan Wedge With New Mass Flux Condition," *Chemical Physics Letters* 830 (2023): 140799.

24. M. I. U. Rehman, H. Chen, and A. Hamid, "Impact of Bioconvection on Darcy–Forchheimer Flow of MHD Carreau Fluid With Arrhenius Activation Energy," *ZAMM—Journal of Applied Mathematics and Mechanics/Zeitschrift für Angewandte Mathematik und Mechanik* 104, no. 1 (2024): e202300164.

25. M. I. U. Rehman, H. Chen, A. Hamid, et al., "Theoretical Investigation of Darcy–Forchheimer Flow of Bioconvection Casson Fluid in the Presence of Chemical Reaction Effect," *Biomass Conversion and Biorefinery* (2022): 1–11.

26. A. M. Hassan, A. A. Alwan, and H. K. Hamzah, "Metallic Foam With Cross Flow Heat Exchanger: A Review of Parameters, Performance, and Challenges," *Heat Transfer* 52, no. 3 (2023): 2618–2650, https://doi.org/10.1002/htj.22798.

27. K. Khanafer, K. Vafai, and M. Lightstone, "Buoyancy-Driven Heat Transfer Enhancement in a Two-Dimensional Enclosure Utilizing Nanofluids," *International Journal of Heat and Mass Transfer* 46, no. 19 (2003): 3639–3653, https://doi.org/10.1016/S0017-9310(03)00156-X.

28. O. Mahian, A. Kianifar, S. Z. Heris, and S. Wongwises, "Natural Convection of Silica Nanofluids in Square and Triangular Enclosures: Theoretical and Experimental Study," *International Journal of Heat and Mass Transfer* 99 (2016): 792–804, https://doi.org/10.1016/j.ijheatmasstransfer.2016.03.045.

29. X. Xin, A. H. Ganie, M. Alwuthaynani, et al., "Parametric Analysis of Pollutant Discharge Concentration in Non-Newtonian Nanofluid Flow Across a Permeable Riga Sheet With Thermal Radiation," *AIP Advances* 144 (2024): 045018.

30. G. C. Bourantas, E. D. Skouras, V. C. Loukopoulos, and V. N. Burganos, "Heat Transfer and Natural Convection of Nanofluids in Porous Media," *European Journal of Mechanics—B/Fluids* 43 (2014): 45–56, https://doi.org/10.1016/j.euromechflu.2013.06.013.

31. H. A. Pakravan and M. Yaghoubi, "Analysis of Nanoparticles Migration on Natural Convective Heat Transfer of Nanofluids," *International Journal of Thermal Sciences* 68 (2013): 79–93, https://doi.org/10.1016/j.ijthermalsci.2012.12.012.

32. D. Wen and Y. Ding, "Formulation of Nanofluids for Natural Convective Heat Transfer Applications," *International Journal of Heat and Fluid Flow* 26, no. 6 (2005): 855–864, https://doi.org/10.1016/j.ijheatfluidflow.2005.10.005.

33. M. I. U. Rehman, H. Chen, and A. Hamid, "Numerical Investigation of Cattaneo–Christov Double Diffusion and Mixed Convection Effects in Non-Darcian Sutterby Nanofluid Using Multi Objective Optimization Through RSM," *International Journal of Hydrogen Energy* 100 (2025): 1219–1230.

34. M. I. U. Rehman, H. Chen, A. Hamid, S. A. Alsallami, A. Al-Zubaidi, and S. Saleem, "Thermal and Solutal Slip Impacts of Tribological Coatings on the Flow and Heat Transfer of Reiner–Philippoff Nanofluid Lubrication Toward a Stretching Surface: The Applications of Darcy–Forchheimer Theory," *Tribology International* 190 (2023): 109038.

35. M. I. U. Rehman, H. Chen, M. I. Khan, A. Hamid, and A. Masmoudi, "Modeling and Predicting Heat Transfer Performance in Bioconvection Flow Around a Circular Cylinder Using an Artificial Neural Network Approach," *Tribology International* 200 (2024): 110182.

36. A. M. Hassan, A. A. Alwan, and H. K. Hamzah, "Numerical Study of Fan Coil Heat Exchanger With Copper-Foam," *International Journal of Fluid Machinery and Systems* 16, no. 1 (2023): 73–88.

37. R. H. Rasheed, A. S. Sadeq, M. N. Fares, S. Salahshour, and R. Sabetvand, "Modeling the Thermal Performance of Hybrid Paraffin–Air Nanostructure in a Heat Sink: Effect of Atomic Ratio of Al_2O_3 Nanoparticles," *Case Studies in Chemical and Environmental Engineering* 11 (2025): 101109.

38. A. B. Ali, S. F. Alhamdi, M. M. Al-Azawii, et al., "Thermal Management in a Phase Change Material-Based Microchannel Heat Sink Manifold System for Cooling Electronic Boards," *Results in Engineering* 26 (2025): 104914.

39. S. A. M. Mehryan, F. M. Kashkooli, M. Ghalambaz, and A. J. Chamkha, "Free Convection of Hybrid Al_2O_3–Cu Water Nanofluid in a Differentially Heated Porous Cavity," *Advanced Powder Technology* 28, no. 9 (2017): 2295–2305, https://doi.org/10.1016/j.apt.2017.06.011.

40. S. Hosseinzadeh, K. Hosseinzadeh, A. Hasibi, and D. D. Ganji, "Thermal Analysis of Moving Porous Fin Wetted by Hybrid Nanofluid With Trapezoidal, Concave Parabolic and Convex Cross Sections," *Case Studies in Thermal Engineering* 30 (2022): 101757, https://doi.org/10.1016/j.csite.2022.101757.

41. M. Ghalambaz, M. A. Sheremet, and I. Pop, "Free Convection in a Parallelogrammic Porous Cavity Filled With a Nanofluid Using Tiwari and Das' Nanofluid Model," *PLoS ONE* 10, no. 5 (2015): e0126486, https://doi.org/10.1371/journal.pone.0126486.

42. T. Groşan, C. Revnic, I. Pop, and D. B. Ingham, "Free Convection Heat Transfer in a Square Cavity Filled With a Porous Medium Saturated by a Nanofluid," *International Journal of Heat and Mass Transfer* 87 (2015): 36–41, https://doi.org/10.1016/j.ijheatmasstransfer.2015.03.078.

43. M. Sheikholeslami, "Numerical Investigation of Nanofluid Free Convection Under the Influence of Electric Field in a Porous Enclosure," *Journal of Molecular Liquids* 249 (2018): 1212–1221, https://doi.org/10.1016/j.molliq.2017.11.141.

44. M. A. Sheremet, T. Grosan, and I. Pop, "Free Convection in a Square Cavity Filled With a Porous Medium Saturated by Nanofluid Using Tiwari and Das' Nanofluid Model," *Transport in Porous Media* 106 (2015): 595–610, https://doi.org/10.1007/s11242-014-0415-3.

45. F. Ali, M. Saqib, I. Khan, and N. Ahmad Sheikh, "Application of Caputo–Fabrizio Derivatives to MHD Free Convection Flow of Generalized Walters'-B Fluid Model," *European Physical Journal Plus* 131, no. 10 (2016): 377, https://doi.org/10.1140/epjp/i2016-16377-x.

46. M. Sheikholeslami, M. Gorji-Bandpy, and D. D. Ganji, "MHD Free Convection in an Eccentric Semi-Annulus Filled With Nanofluid," *Journal of the Taiwan Institute of Chemical Engineers* 45, no. 4 (2014): 1204–1216, https://doi.org/10.1016/j.jtice.2014.03.010.

47. A. M. Alqahtani, M. Bilal, A. Ali, H. A. E. W. Khalifa, and H. Alqahtani, "Numerical Calculation of Unsteady MHD Nanofluid Flow Across Two Fluctuating Discs With Chemical Reaction and Zero Mass Flux," *ZAMM—Journal of Applied Mathematics and Mechanics/Zeitschrift für Angewandte Mathematik und Mechanik* 1043 (2024): e202300001.

48. M. I. U. Rehman, H. Chen, A. Hamid, et al., "Effect of Cattaneo–Christov Heat Flux Case on Darcy–Forchheimer Flowing of Sutterby Nanofluid With Chemical Reactive and Thermal Radiative Impacts," *Case Studies in Thermal Engineering* 42 (2023): 102737.

49. M. I. Ur Rehman, H. Chen, and A. Hamid, "Multi-Physics Modeling of Magnetohydrodynamic Carreau Fluid Flow With Thermal Radiation and Darcy–Forchheimer Effects: A Study on Soret and Dufour Phenomena," *Journal of Thermal Analysis and Calorimetry* 148, no. 24 (2023): 13883–13894.

50. M. A. Alomari, A. M. Hassan, A. Alajmi, A. M. Sadeq, F. Alqurashi, and M. A. Flayyih, "A Comprehensive Numerical Analysis of Heat Transfer Enhancement in NEPCM–Water Mixtures Using Oscillating Fin and Oriented Magnetic Fields," *International Communications in Heat and Mass Transfer* 161 (2025): 108455, https://doi.org/10.1016/j.icheatmasstransfer.2024.108455.

51. K. Ghasemi and M. Siavashi, "MHD Nanofluid Free Convection and Entropy Generation in Porous Enclosures With Different Conductivity Ratios," *Journal of Magnetism and Magnetic Materials* 442 (2017): 474–490, https://doi.org/10.1016/j.jmmm.2017.07.028.

52. M. Sheikholeslami, "Influence of Magnetic Field on Nanofluid Free Convection in an Open Porous Cavity by Means of Lattice Boltzmann Method," *Journal of Molecular Liquids* 234 (2017): 364–374, https://doi.org/10.1016/j.molliq.2017.03.104.

53. A. J. Chamkha and A. M. Aly, "MHD Free Convection Flow of a Nanofluid Past a Vertical Plate in the Presence of Heat Generation or Absorption Effects," *Chemical Engineering Communications* 198, no. 3 (2010): 425–441, https://doi.org/10.1080/00986445.2010.520232.

54. A. Y. Ghaly, "Solitons and Fractals, Radiation Effects on a Certain MHD Free-Convection Flow," *Chaos, Solitons & Fractals* 13, no. 9 (2002): 1843–1850, https://doi.org/10.1016/S0960-0779(01)00193-X.

55. M. A. Kumar, Y. D. Reddy, V. S. Rao, and B. S. Goud, "Thermal Radiation Impact on MHD Heat Transfer Natural Convective Nano Fluid Flow Over an Impulsively Started Vertical Plate," *Case Studies in Thermal Engineering* 24 (2021): 100826, https://doi.org/10.1016/j.csite.2020.100826.

56. M. Ghalambaz, A. Doostani, E. Izadpanahi, and A. J. Chamkha, "Conjugate Natural Convection Flow of Ag–Mgo/Water Hybrid Nanofluid in a Square Cavity," *Journal of Thermal Analysis and Calorimetry* 139 (2020): 2321–2336, https://doi.org/10.1007/s10973-019-08617-7.

57. S. Ahmad, B. M. Cham, D. Liu, S. U. Islam, M. A. Hussien, and H. Waqas, "Numerical Analysis of Heat and Mass Transfer of MHD Natural Convection Flow in a Cavity With Effects of Source and Sink," *Case Studies in Thermal Engineering* 53 (2024): 103926, https://doi.org/10.1016/j.csite.2023.103926.

58. M. Usman, Z. H. Khan, and M. B. Liu, "MHD Natural Convection and Thermal Control Inside a Cavity With Obstacles Under the Radiation Effects," *Physica A: Statistical Mechanics and its Applications* 535 (2019): 122443, https://doi.org/10.1016/j.physa.2019.122443.

59. M. A. Alomari, K. Al-Farhany, Q. H. Al-Salami, et al., "Magnetohydrodynamic Mixed Convection in Lid-Driven Curvilinear Enclosure With Nanofluid and Partial Porous Layer," *Journal of Magnetism and Magnetic Materials* 582 (2023): 170952, https://doi.org/10.1016/j.jmmm.2023.170952.

60. T. Basak, S. Roy, T. Paul, and I. Pop, "Natural Convection in a Square Cavity Filled With a Porous Medium: Effects of Various Thermal Boundary Conditions," *International Journal of Heat and Mass Transfer* 49, no. 7–8 (2006): 1430–1441, https://doi.org/10.1016/j.ijheatmasstransfer.2005.09.018.

61. M. Sheikholeslami, T. Hayat, and A. Alsaedi, "MHD Free Convection of Al_2O_3–Water Nanofluid Considering Thermal Radiation: A Numerical Study," *International Journal of Heat and Mass Transfer* 96 (2016): 513–524.

62. R. A. Hussein, A. M. Hassan, and R. H. Hameed, "Mixed Convection Heat Transfer in a Partial Porous Layered Split Lid-Driven Wavy Wall Cavity With Cu–H_2O Nanofluid," *Numerical Heat Transfer, Part B: Fundamentals* (2024): 1–27, https://doi.org/10.1080/10407790.2024.2343329.

63. A. Bejan and J. Kestin, "Entropy Generation Through Heat and Fluid Flow," *ASME Journal of Applied Mechanics* 50, no. 2 (1983): 475, https://doi.org/10.1115/1.3167071.

64. N. Z. Khan, S. Bilal, L. Kolsi, A. S. Shflot, and M. Y. Malik, "A Case Study on Entropy Generation in MHD Nanofluid Flow in L-Shaped Triangular Corrugated Permeable Enclosure," *Case Studies in Thermal Engineering* 59 (2024): 104487, https://doi.org/10.1016/j.csite.2024.104487.

65. M. A. Alomari, K. Al-Farhany, A. L. Hashem, M. F. Al-Dawody, F. Redouane, and O. A. Olayemi, "Numerical Study of MHD Natural Convection in Trapezoidal Enclosure Filled With (50% MgO–50% Ag/Water) Hybrid Nanofluid: Heated Sinusoidal From Below," *International Journal of Heat & Technology* 39, no. 4 (2021): 1271–1279, https://doi.org/10.18280/ijht.390425.

66. M. Hemmat Esfe, A. A. Abbasian Arani, M. Rezaie, W.-M. Yan, and A. Karimipour, "Experimental Determination of Thermal Conductivity and Dynamic Viscosity of Ag–Mgo/Water Hybrid Nanofluid," *International Communications in Heat and Mass Transfer* 66 (2015): 189–195, https://doi.org/10.1016/j.icheatmasstransfer.2015.06.003.

67. C.-L. Chen and C.-H. Cheng, "Experimental and Numerical Study of Mixed Convection and Flow Pattern in a Lid-Driven Arc-Shape Cavity," *Heat and Mass Transfer* 41 (2004): 58–66, https://doi.org/10.1007/s00231-004-0541-5.

68. M. F. Al-Dawody, A. M. Hassan, N. H. Hamza, M. A. Theeb, M. Ghalambaz, and M. Sheremet, "Investigation of Hydro-Thermal Behavior of Two Immiscible Fluids in a Wavy Cavity Subjected to an Inclined Magnetic Field and Heat Flux," *International Journal of Thermofluids* 26 (2025): 101081.